Fuel 428 (2027) 140022

Contents lists available at ScienceDirect

Fuel

journal homepage: www.elsevier.com/locate/fuel

Full Length Article

Integrated biomass–geothermal system for decarbonized ammonia production enhanced by a supercritical CO_2 cycle: a data-driven approach

Marwa Ben Slimene [a], Ali Basem [b], Naeim Farouk [c,*], Mohd Abul Hasan [d], Mohamed Arbi Khlifi [e,*], Saiful Islam [d], Zukhra Atamuratova [f,g], Otabek Mukhitdinov [h], Egambergan Khudoynazarov [i], Ibrahim Mahariq [j,k,l,*]

[a] Department of Computer Engineering, College of Computer Science and Engineering, University of Ha'il, P.a Box 2440, Ha'il City, Saudi Arabia
[b] Advanced Technical College, University of Warith Al-Anbiyaa, Karbala, Iraq
[c] Mechanical Engineering Department, College of Engineering in Al-Kharj, Prince Sattam Bin Abdulaziz University, Al-Kharj 11942, Saudi Arabia
[d] Civil Engineering Department, College of Engineering, King Khalid University, Abha 61421, Saudi Arabia
[e] Department of Electrical Engineering, Faculty of Engineering, Islamic University of Madinah, Madinah 42351, Saudi Arabia
[f] National Research University TIIAME, Kori Niyoziy 39, Tashkent 100000, Uzbekistan
[g] University of Tashkent for Applied Sciences, Str. Gavhar 1, Tashkent 100149, Uzbekistan
[h] Kimyo International University in Tashkent, Shota Rustaveli Str. 156, Tashkent 100121, Uzbekistan
[i] Mamun University, Bolkhovuz Street 2, Khiva 220900, Uzbekistan
[j] Department of Electrical and Electronic Engineering, Faculty of Engineering and Architecture, Istanbul Gelisim University, Avcılar-Istanbul, 34310, Istanbul, Turkiye
[k] Department of Medical Research, China Medical University Hospital, China Medical University, Taichung, Taiwan
[l] University College, Korea University, Seoul 02481, South Korea

ARTICLE INFO

Keywords:
Ammonia production
Biomass gasification
Supercritical CO_2 brayton cycle
Decarbonization pathways
Techno-economic assessment
Particle swarm optimization (PSO)

ABSTRACT

Ammonia's emergence as a carbon-free energy carrier calls for pathways that decarbonize both its synthesis and the electricity that powers it. This work proposes a hybrid biomass–geothermal platform for electricity and ammonia production. The configuration couples a gas turbine fueled by biomass-derived syngas with a supercritical CO_2 Brayton cycle, a dual-flash geothermal configuration, and an ammonia synthesis loop. A comprehensive exergy accounting is performed alongside an environmental and techno-economic evaluation. Exergy destruction is dominated by the gas turbine and gasification train (70.6%, 4148.95 kW), followed by the geothermal subsystem (1188.14 kW) and the supercritical CO_2 cycle (297.5 kW). A multidimensional parametric analysis is conducted to evaluate the sensitivity of system performance indicators to key decision variables. The split ratio of the supercritical CO_2 cycle exhibits a non-monotonic influence on system behavior: both efficiency and net power generation increase until a split ratio of 0.74, beyond which thermodynamic mismatches reduce system performance. Under favorable geothermal temperature and pressure conditions, normalized CO_2 emissions decrease to 28.47 kg/GJ. Conversely, increasing the gas turbine inlet temperature raises the levelized cost of electricity by up to 41%, while simultaneously reducing efficiency and increasing emissions. To efficiently explore the design space, artificial neural network surrogate models are integrated with a multi-objective particle swarm optimization algorithm. The optimal solution yields an exergy efficiency of 54.68%, an ammonia production rate of 592.9 kg/day, and a levelized cost of electricity of 6.47 cents/kWh. Scenario analysis indicates that the project net present value ranges from \$2.29 million under conservative price assumptions to \$6.53 million under favorable market conditions.

1. Introduction

The transition toward low-carbon and flexible energy systems has become a global priority in response to escalating climate concerns, fossil fuel depletion, and the pressing need for energy security [1]. According to the International Energy Agency's Global Energy Review 2025, carbon dioxide (CO_2) emissions resulting from fuels combustion and industrial processes increased by 0.8% in 2024, reaching a record 37.8 gigatonnes (Gt), with energy-related sectors continuing to account

* Corresponding authors.
E-mail addresses: n.mohammed@psau.edu.sa (N. Farouk), medarbi@iu.edu.sa (M.A. Khlifi), ibmahariq@gmail.com (I. Mahariq).

https://doi.org/10.1016/j.fuel.2026.140022
Received 13 December 2025; Received in revised form 21 March 2026; Accepted 22 May 2026
Available online 19 June 2026

Nomenclature

A	Surface area (m^2)
AS	Annual saving ($)
AI	Annual income ($)
$\dot{E}x$	Exergy rate (kW)
$\dot{E}x_D$	Exergy destruction rate (kW)
ex	Exergy per unit mass (kJ/kg)
h	Specific enthalpy (kJ/kg)
c	Cost per unit exergy ($ /GJ)
$\dot{C}$	Cost rate ($/h)
$CEPCI$	Chemical engineering plant cost index, (−)
CRF	Capital recovery factor (−)
FC	Fixed cost ($)
G	Gibbs free energy (kJ/mol)
h	Enthalpy per unit of mass (kJ/kg)
i	Interest rate (−)
LHV	Lower heating value (kJ/kg)
$\dot{m}$	Rate of mass flow (kg/s)
MC	Moisture content (g/m^3)
n	Lifespan of the system
N	Operational years
PP	Payback period (Year)
$\dot{Q}$	Heat transfer rate (kW)
R	Overall ohmic resistance (Ω)
s	Specific entropy (kJ/kg K)
τ	Operation time (h)
T	Temperature (°C)
V	Voltage (V)
$\dot{W}$	Power generation (kW)
Z	Purchase cost ($)
$\dot{Z}$	Overall cost rate ($/s)
ΔT	Temperature difference (°C)
ΔH	Change in enthalpy (kJ)
ΔG	Variation in Gibbs energy (kJ)

Subscripts

0	Reference state
a	Anode
ch	Chemical
$Comp.$	Compressor
$Comb.$	Combustion
c	Cathode
$elec$	Elctricity
e	Exit
EV	Expansion valve
f	Formation
$Geofluid$	Geothermal fluid
In	Inlet
ph	Physical
V	Valve

Greek Symbols

β	Ratio of chemical exergy
w	Number of atoms of the moisture
η	Efficiency
φ	Maintenance factor

Abbreviation

AC	Air compressor
AT	Air turbine
AP	Air preheater
APR	Ammonia production rate
ANN	Artificial neural network
DFGC	Dual-flash geothermal cycle
EE	Exergy efficiency
FC	Flash chamber
GT	Gas turbine
GTIT	Gas turbine inlet temperature
HEX	Heat exchanger
HRES	Hybrid renewable energy system
LCOE	Levelized cost of electricity
LNG	Liquefied natural gas
NE	Normalized emissions
NPG	Net power generation
NPV	Net present value
MC	Moisture content
PSO	Particle swarm optimization

for the overwhelming majority of these emissions [2]. This underscores the persistent dominance of the energy system as the primary source of global CO_2 output. Traditional stand-alone renewable energy systems often face challenges such as inherent intermittency, time-dependent operation, and high costs, necessitating complementary technologies to ensure reliability—particularly in off-grid or industrial-scale applications [3,4]. Hybrid renewable energy systems, which incorporate several energy sources and energy vectors, have emerged as a promising pathway to increase energy efficiency, system resilience, and multi-functionality [5]. Among the diverse options, systems that combine dispatchable renewables (like biomass and geothermal) with advanced thermodynamic cycles and power-to-fuel pathways offer unique potential for both power generation and fuel production in a carbon–neutral framework.

The conceptual foundation of hybrid renewable energy systems (HRESs) lies in the strategic combination of energy resources to compensate for the limitations of individual technologies. Early generations of HRESs primarily focused on pairing intermittent renewables—such as solar and wind—with fossil fuels or batteries to ensure dispatchability [6]. However, recent technological and environmental shifts have driven interest toward renewable–renewable hybrids, which leverage the complementary characteristics of different natural resources. For instance, the constant thermal output of geothermal energy can stabilize variable energy inputs from other sources [7], while biomass offers a controllable, carbon–neutral feedstock for on-demand electricity and heat production [8,9]. These synergies have led to a new generation of hybrid configurations aimed at maximizing both energy output and exergy efficiency through intelligent thermal and material integration.

In this context, Olabi et al. [10] highlighted the increasing integration of geothermal energy with solar systems, noting that 45% of geothermal hybrids incorporate solar energy, mainly for heating and cooling applications. Similarly, Fedakar et al. [11] compared hybrid geothermal–solar systems with standalone photovoltaic (PV)-battery setups in Türkiye, concluding that although geothermal–solar hybrids exhibit lower emissions and levelized costs of electricity, their scalability is geographically constrained. Beyond solar-geothermal coupling, Hai et al. Hai et al. [12] proposed two innovative biomass–geothermal hybrid configurations, showing that direct steam injection into turbines significantly improves exergy efficiency and reduces environmental impacts. These findings support the notion that hybridization can be tailored to local resource availability while enhancing performance metrics. Further broadening the scope, Toker [13] developed a multi-output system integrating solar, geothermal, and supercritical CO_2 cycles, capable of simultaneously producing electricity, hydrogen, heating, cooling, and water with energetic and exergetic efficiencies exceeding 50%. An et al. [14] took a similar approach by using biomass combustion to superheat geofluid in a multigeneration plant, demonstrating both thermodynamic and economic benefits under optimized conditions. The potential of geothermal–biomass synergy has also been reviewed by Zhang et al. [15], who emphasized its versatility across electricity generation, hydrogen production, and refrigeration applications. The value of these renewable–renewable hybrids become even more evident in remote or extreme environments [16]. Geng et al. [17] validated the feasibility of combining PV, wind energy, and ground-source heating pump in isolated areas, achieving a 95% renewable energy fraction and a competitive levelized cost of electricity. Likewise, Afshardoost and Shamsi [18] demonstrated that integrating biomass gasification with geothermal systems could support large-scale green hydrogen and power production with exergy efficiencies above 65% and substantial environmental savings. These studies collectively illustrate that hybridization is not merely a technical convenience but a strategic pathway toward more robust, flexible, and decarbonized energy systems. As Kaur et al. [19] concluded in their systematic review, hybrid configurations that integrate hydrogen, biomass, and intelligent energy management systems are essential to overcoming intermittency, reducing emissions, and achieving long-term energy resilience.

In parallel with these developments, the role of multi-generation and multi-vector energy systems has become increasingly prominent. Rather than focusing solely on electricity generation, next-generation systems aim to co-produce heat, power, hydrogen, and chemical fuels within a single operational architecture [20]. This approach aligns with the principles of sector coupling and integrated energy planning, allowing systems to address multiple demands across power, mobility, and industrial applications. For instance, Hai et al. [21] developed a biomass-fueled multigeneration framework that leverages Brayton cycles alongside humidification-dehumidification to concurrently generate electricity and freshwater, achieving energy efficiency of 75.8% and exergy efficiency of 37%. In a similar direction, Yan et al. [22] proposed a geothermal/biomass-powered system capable of co-producing power, methanol, and hydrogen, with notable exergetic efficiency and economic viability enhanced through multi-objective optimization. Rabet et al. [23] expanded this scope by incorporating desalination into a biomass-geothermal hybrid platform, yielding over 5400 kW of electricity and 72.36 kg/s of clean water while applying multi-criteria optimization to balance cost and efficiency trade-offs. The integration of hydrogen production has also gained traction. Özen and Çağlı [24] introduced a biomass-geothermal hybrid system using a proton exchange membrane (PEM) electrolyzer, optimizing performance through advanced exergy analysis to reduce product costs by nearly 50%. Similarly, Yu et al. [25] presented a platform combining biomass gasification, oxy-fuel combustion, and molten carbonate fuel cells to deliver electricity, cooling, and freshwater—while achieving high exergetic efficiency and a payback period under two years. Beyond electricity and hydrogen, compressed air energy storage (CAES) has been coupled with biomass systems to enhance seasonal flexibility in power and heat supply. Xue et al. [26] reported that such a hybrid system maintained exergy efficiencies above 76% year-round and achieved a 4.45-year payback period. Furthermore, Bai et al. [27] demonstrated the potential of geothermal-biomass hybrids for cogenerating electricity and freshwater, reporting over 44% exergetic efficiency and low CO_2 emissions.

A critical enabler of shift toward multi-output, low-carbon energy systems is the integration of advanced thermodynamic cycles—such as the supercritical CO_2 (S-CO_2) Brayton cycle—which can operate efficiently at high temperatures and recover low-grade waste heat [28,29]. When combined with renewable-driven electrolysis and synthetic fuel production, these systems form the backbone of a circular, decarbonized energy economy. By layering syngas-fired recompression Brayton cycles with S-CO_2 and geothermal-driven flash-binary loops, Lv et al. [30] introduced a hierarchically cascaded hybrid system for generating power and heat. By applying multi-objective optimization, the system demonstrated a synergistic boost in performance—achieving over 44% exergy efficiency and strong economic returns. Hamida et al. [31] introduced a forward-looking hybrid energy architecture combining solar heliostat fields, an S-CO_2 cycle, smart CAES, and hydrogen generation via PEM electrolysis. Designed for high-irradiance regions, the system leverages seasonal energy shifting and advanced optimization to achieve high efficiency (47.9%), substantial net power output (76.3 MW), and economic viability. Abdelghafar et al. [32] reviewed direct integration of S-CO_2 cycles with concentrating solar power (CSP), showing efficiency improvements up to 60% and reduced system costs. They emphasized the potential of hybridizing with geothermal or biomass to enhance flexibility, while identifying research gaps in real-world performance and hybrid system design. Zhu et al. [33] proposed a biomass–geothermal hybrid framework integrating S-CO_2 and Kalina cycles, achieving enhanced thermal utilization. The system delivered combined power, heat, and cooling with 6.87-years payback period and 23.08% exergetic efficiency.

Another emerging trend is the incorporation of power-to-X technologies, particularly green hydrogen and ammonia production, into renewable energy systems [34]. Hydrogen is increasingly seen as a key energy carrier for long-term storage and industrial decarbonization [35], while ammonia offers the added benefit of high energy density and easier transport [36]. Recent advancements in PEM electrolyzers and modular ammonia synthesis have opened new possibilities for embedding these technologies directly into hybrid energy platforms [37]. This not only enables energy storage and fuel production during periods of surplus generation but also provides grid-balancing capabilities and potential for energy export.

Recent studies reflect this shift toward deeply integrated, multi-vector energy systems. For instance, biomass–geothermal– solar multi-generation plant was developed by Bozgeyik et al. [38] producing hydrogen, electricity, heat, freshwater, and cooling achieving exergy efficiency exceeding 27% with a hydrogen generation rates of 3.52 kg/h, while highlighting the value of multi-input configurations in maximizing system outputs. Focusing on feedstock pathways, Wang et al. [39] conducted a bibliometric review of biomass-based hydrogen production, concluding that technologies like gasification and steam reforming can now deliver hydrogen at competitive costs (<2 $/kg) with over 90% emissions reduction, making biomass a promising route in hybrid designs. A geothermal–biomass hybrid system optimized by Yin [40] showcased hydrogen and ammonia co-production, delivering over 500 kg/day of ammonia with favorable environmental and economic metrics, and emphasized ammonia's role as a flexible energy storage medium. In another study, Yilmaz [41] proposed a geothermal multi-generation plant that integrates a transcritical CO_2 Rankine cycle with a hydrogen production unit. The system achieved energy and exergy efficiencies of 27.60% and 22.56%, respectively. The optimal total plant cost rate was reported as 80.48 $/h.

The integration of ammonia synthesis into hybrid systems has also gained momentum. Khoshgoftar Manesh et al. [42] designed a tri-renewable system (solar–wind–biomass) that co-produces steam, power, and ammonia, using syngas as both a fuel and synthesis input, and achieved an ammonia output exceeding 275 tons/day. Similarly, Shamsi et al. [43] suggested a geothermal-based polygeneration system that produced ammonia, hydrogen, electricity, and thermal utilities. The system achieved a payback period of just 3 years with an energy efficiency of 50%. Another example by Tang et al. [44] combined geothermal heat and ammonia-fueled solid oxide fuel cells for electricity and cooling, showing that ammonia not only acts as a storable fuel but also improves the flexibility and dispatchability of renewable-based systems. Broader polygeneration frameworks are also exploring ammonia and hydrogen integration. Yilmaz et al. [45] analyzed an integrated geothermal system that combines an ORC, PEM electrolysis, ammonia synthesis, and desalination. The integration achieved energy and exergy efficiencies of 26.31% and 33.09%, respectively. It also enabled the simultaneous production of electricity, hydrogen, ammonia, and desalinated water. Jia et al. [46] developed a configuration producing power, heating, cooling, and ammonia using modified Kalina and organic Rankine cycle (ORC) sections alongside geothermal sources, reporting high energy and exergy efficiencies (34.55% and 57.17%). Meanwhile, Khoshgoftar Manesh et al. [47] emphasized the systemic and ecological aspects of polygeneration systems by integrating biomass–solar–wind platforms to produce 10.1 MW power, 17.75 tons/day ammonia, and 523 m^3/day freshwater, underscoring the role of advanced design and management in enabling sustainable, multi-output systems.

A considerable body of research has been devoted to improving the sustainability of energy and fuel production through the utilization of renewable resources and advanced energy conversion technologies. Biomass-based systems have been widely investigated for their capability to produce electricity, heat, and value-added fuels, and numerous thermodynamic studies have examined their performance through energy and exergy analyses. In parallel, geothermal energy has attracted increasing attention as a reliable renewable resource for continuous power generation. However, most existing studies have been conducted within specific technological contexts and have generally relied on conventional parametric approaches to evaluate system performance. Building upon these developments, the present study proposes a multi-generation framework that combines geothermal energy and biomass gasification with an S-CO_2 Brayton cycle, PEM electrolysis, and an ammonia synthesis unit for the simultaneous production of electrical power and clean fuel. The hybrid configuration exploits the complementary characteristics of geothermal and biomass resources to enhance system reliability and operational flexibility. The performance of the proposed system is investigated through a comprehensive parametric analysis to examine the sensitivity of key performance indicators—including net power generation, ammonia production rate, exergy efficiency, normalized CO_2 emissions, levelized cost of electricity (LCOE), and sustainability index—to major operating parameters. The results reveal notable nonlinear effects associated with the S-CO_2 split ratio, which introduces important thermodynamic trade-offs within the cycle. Furthermore, to capture the complex interactions between operating variables and system performance indicators, a data-driven optimization framework is developed by coupling artificial neural network (ANN) surrogate models with a multi-objective particle swarm optimization (MOPSO) algorithm.

A feature-based comparison of representative studies from the literature is presented in Table 1 to highlight the main system components and methodological approaches considered in previous works and to clarify the contributions of the present study.

2. System description

The designed multi-energy renewable energy system integrates biomass conversion, geothermal energy extraction, and hydrogen–ammonia production, forming a multi-functional, intergenerational configuration aimed at maximizing energy efficiency and fuel flexibility. The system architecture comprises three major subsystems: (1) a biomass-powered Brayton cycle (BC) and an S–CO_2 recompression Brayton cycle, (2) a geothermal energy configuration, and (3) a hydrogen and ammonia synthesis unit. These subsystems are thermally coupled in a complementary manner to improve internal energy recovery and system performance. An overall schematic of the proposed configuration, including the key components and energy flow pathways across all subsystems, is illustrated in Fig. 1. The integration of geothermal and biomass resources in the proposed system is motivated by their complementary operational and thermodynamic characteristics. Geothermal energy represents a stable and continuous renewable heat source that can support base-load power generation. However, its relatively moderate temperature levels may limit its applicability in certain high-temperature processes. In contrast, biomass gasification provides a dispatchable energy source capable of delivering higher-temperature thermal energy as well as chemical energy in the form of syngas. By combining these two resources, the proposed system benefits from the operational stability of geothermal energy while utilizing biomass to enhance temperature levels, operational flexibility, and fuel production capability.

The procedure commences with biomass (State 1) introduced into a downdraft gasifier, where it reacts with compressed air (State 3) supplied by Compressor 3. The resulting syngas (State 4) is channeled to the combustion chamber (CC), wherein it is combusted to generate flue gases with high-temperature. Simultaneously, ambient air (State 5) is introduced into Compressor 1 for initial pressurization. The compressed air (State 6) then passes through an intercooler (IC) and is further pressurized in Compressor 2, exiting at a higher pressure level (State 7). The air preheater (AP) preheats this air using the return stream from the gas turbine (GT) (State 12), producing a high-energy stream (State 9) that expands in the air turbine (State 10). The expanded air is reheated inside the CC and subsequently expanded again within the gas turbine (State 11–12), producing mechanical work and electrical power. The exhaust gas (State 12) then flows back to the AP for regenerative heating.

Instead of releasing the thermal energy of the exhaust from gas turbine, the system recovers it to drive a recompression S–CO_2 Brayton cycle. Two recuperators— a high-temperature recuperator (HTR) and a low-temperature recuperator (LTR)—are employed in this cycle's split-flow configuration. One portion of the CO_2 stream is cooled and compressed to high pressure by the main compressor (MC), while the other is compressed directly by the recompressor (RC). The two streams merge

Table 1
Literature approaches compared with the current study.

Feature	Studies				
	Geothermal power studies	Biomass-based energy systems	Hybrid renewable energy systems	Power-to-ammonia systems	This study
Subsystems	Geothermal power cycle (ORC/flash)	Biomass gasification or combustion systems	Hybrid renewable power systems (e.g., solar–wind–biomass)	Electrolysis + ammonia synthesis loop	S-CO_2 Brayton cycle + biomass gasification + PEM electrolysis + ammonia synthesis
Thermal integration	Limited to geothermal power cycle	Heat recovery within biomass conversion section	Limited thermal coupling between renewable sources	Mainly process-level heat recovery	Heat integration linking the power, hydrogen, and ammonia production units
Energy sources	Geothermal energy	Biomass feedstock	Multiple renewable sources (solar, wind, biomass, geothermal)	Renewable electricity	Hybrid geothermal energy + biomass resources
Fuel production	Hydrogen (gas or liquid)	Hydrogen via reforming or gasification	Hydrogen/ammonia	Core subsystem (electrolysis)	Integrated PEM water electrolysis and Haber–Bosch synthesis
Power cycle technology	ORC, steam Rankine cycle, flash or dual flash units	Steam cycle or direct heat use	Kalina cycle, ORC, Stean Rankine cycle, Dual loop organich flash cycle	External electricity supply	Supercritical CO_2 Brayton cycle; High efficiency, compact turbomachinery

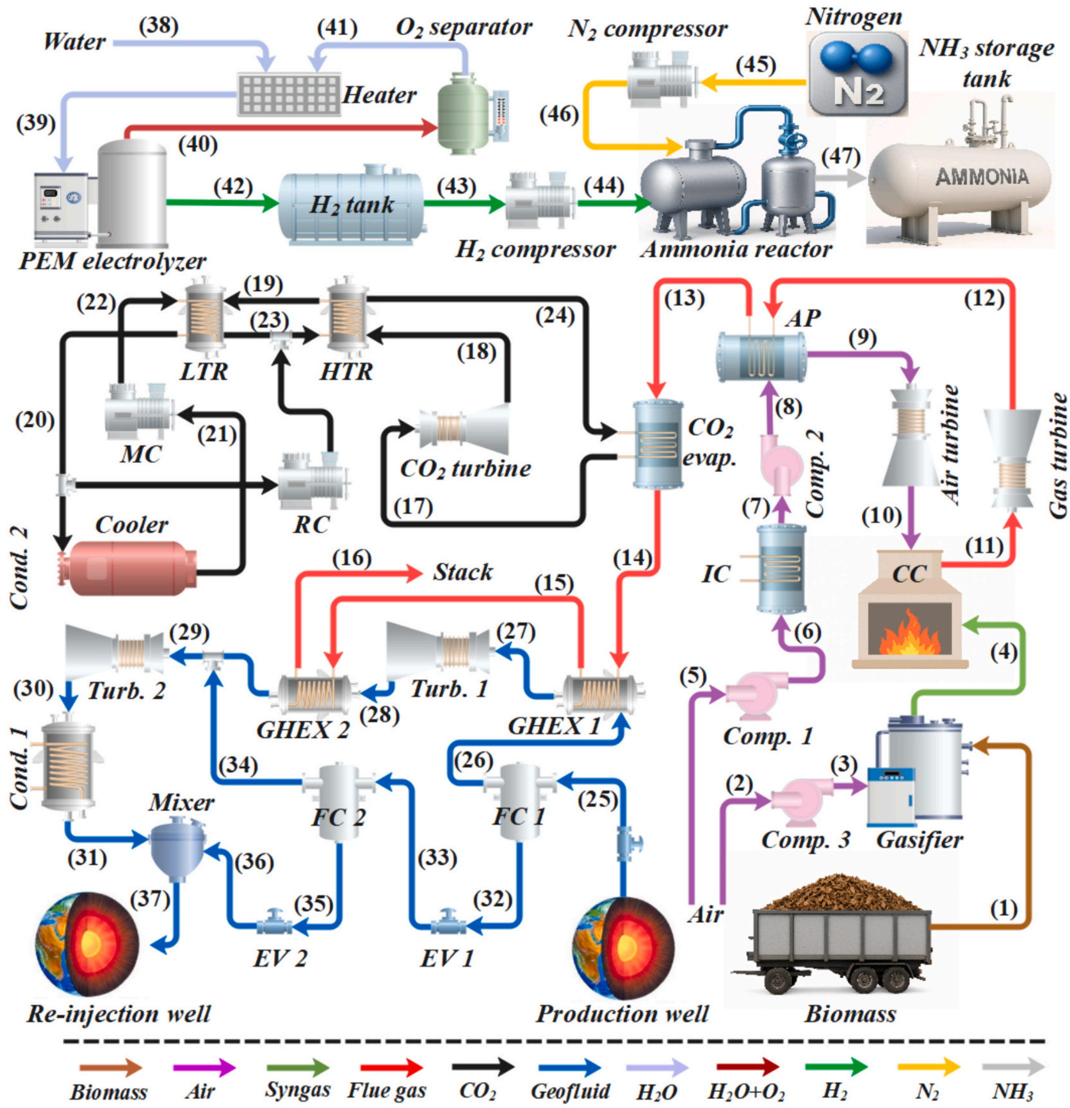

Fig. 1. Overview of the proposed hybrid renewable energy system integrating biomass, geothermal, and hydrogen–ammonia production subsystems.

at State 23, are reheated in the HTR, and are then expanded in the CO_2 turbine, generating additional power from recovered waste heat. Fig. 2 depicts the corresponding temperature-entropy (T–S) graph for this cycle.

The flue gas exiting the CO_2 evaporator still retains significant thermal energy, which the system utilizes to boost the performance of a dual-flash geothermal configuration (DFGC). The geothermal fluid passes through the first flash chamber (FC1), where it separates into two streams (States 26 and 32). Stream 26 is reheated via the first geothermal heat exchanger (GHEX1) and then expanded in Turbine 1, generating power. The resulting stream (State 28) is reheated again using GHEX2, which extracts the remaining energy from the exhaust gas. This reheated stream is then mixed with fluid from the second flash chamber (FC2) and expanded within the Turbine 2 (State 29–30) to generate further power.

To enhance energy storage and system flexibility, a hydrogen and ammonia production module is incorporated. Excess electricity from the power generation cycles is supplied to a PEM electrolyzer, which splits water into hydrogen and oxygen. The produced hydrogen (State 42) is compressed and stored, while nitrogen from the ambient air separation unit (ASU) is compressed separately (State 46). Producing nitrogen via cryogenic separation is beneficial since the process scales well and yields nitrogen of high purity. These two gases (States 42 and 46) are then fed into an ammonia synthesis reactor, where ammonia is produced and subsequently stored in a dedicated tank (State 47). This fuel synthesis pathway enables surplus energy to be stored chemically, increasing the system's flexibility and dispatchability. By leveraging the cascading thermal gradients and integrating power and fuel subsystems, the proposed configuration achieves a high degree of energy utilization and system synergy. The complementarity between the biomass, geothermal, and hydrogen–ammonia cycles results in a compact, efficient, and renewable energy platform capable of multi-output production.

The following guide provides a concise review about each state, emphasizing the principal processes in each level:

- States 1–13: Biomass-fed gas turbine cycle for electricity generation.
- States 17–24: Supercritical CO_2 recompression Brayton cycle.
- States 25–37: DFGC for multi-stage electricity production.
- States 38–43: PEM electrolyzer utilizing extra electricity to produce hydrogen.
- States 44–47: Ammonia synthesis cycle converting H_2 and N_2 into ammonia.

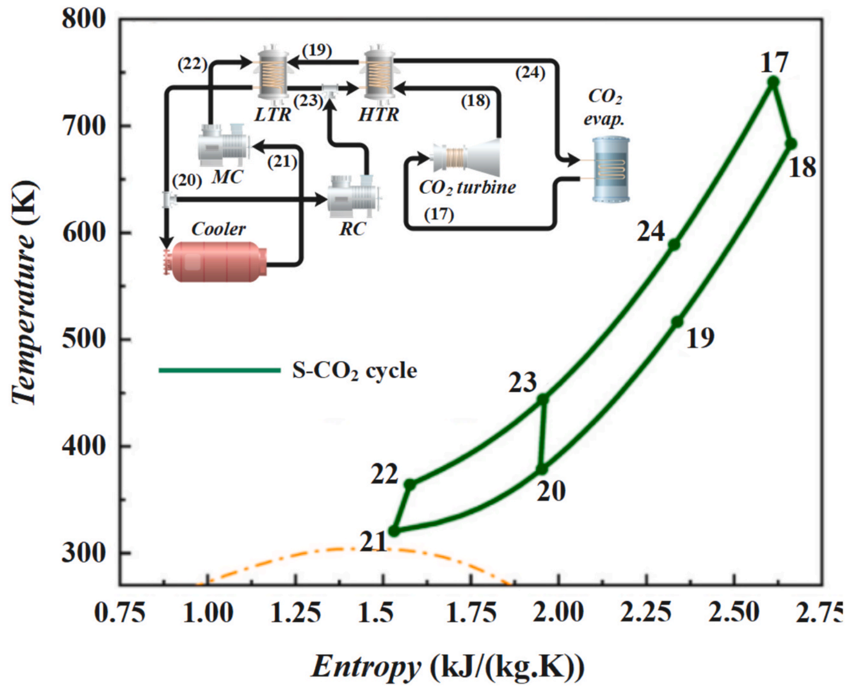

Fig. 2. Temperature–entropy (T–S) graph of the S-CO_2 cycle integrated within the proposed system.

3. Methodology

This section outlines the modeling strategy adopted to assess the energy, exergy, environmental, and economic performance of the proposed model. A detailed framework is developed to simulate the system functioning under realistic operating settings, drawing upon thermodynamic principles and cost analysis techniques.

3.1. Assumptions

To streamline the analysis and maintain consistency, several simplifying assumptions are made, as described below:

- All system components operate under steady-state and steady-flow conditions.
- Changes in potential and kinetic energy of working fluids are considered negligible throughout the system.
- Mechanical losses and frictional pressure drops across piping and ducts are not considered.
- The external environment for exergy calculations is defined at the reference pressure of 1 atm and a temperature of 25 °C.
- The mole fraction of nitrogen (N_2) and oxygen (O_2) in atmospheric air is 79% and 21%, respectively, making it a binary gas mixture.
- The gasification process is assumed to proceed efficiently, reaching thermodynamic equilibrium due to adequate residence time and reaction kinetics.
- The syngas exiting the gasifier is considered to have the same temperature as the gasification zone.

3.2. Simulation

The modeling method employed to represent the primary subsystems' operational behavior and their interconnections in the hybrid energy setup is outlined in detail in this section. The objective is to replicate the framework's thermodynamic, economic, and environmental performance through a series of integrated models developed for each major component and their coupled processes.

3.2.1. Biomass gasification

In this study, gasification is approximated by a non-stoichiometric equilibrium model, assuming the interaction of biomass with water vapor and a precisely metered quantity of oxidizing agent. The general form of the gasification reaction is expressed as [48,49]:

$$CH_aO_b\ N_c + wH_2O + m(O_2 + 3.76\ N_2) \rightarrow n_1H_2 + n_2CO + n_3CO_2 + n_4H_2O + n_5CH_4 + n_6\ N_2 \tag{1}$$

In this equation, w and m refer to the molar quantities of steam and oxidizer, respectively, and the terms n_1 through n_6 denote the molar outputs of the product gases. The molar quantity of water vapor introduced (w) is calculated based on the feedstock's moisture content (MC), using the relationship [48]:

$$w = \frac{M_{\text{biomass}} \times MC}{M_{H_2O} \times (1 - MC)} \tag{2}$$

here M_{H_2O} and M_{biomass} are the molar masses of the water and dry biomass, respectively. Also, MC is determined as:

$$MC = \frac{\text{Water Mass}}{\text{Wet Biomass Mass}} \tag{3}$$

To determine syngas composition, several fundamental reactions that reach equilibrium within the gasifier are considered. These reactions include [48]:

$$C + CO_2 \leftrightarrow 2CO \tag{4}$$

$$C + H_2O \leftrightarrow CO + H_2 \tag{5}$$

$$C + 2H_2 \leftrightarrow CH_4 \tag{6}$$

$$CO + H_2O \leftrightarrow CO_2 + H_2 \tag{7}$$

Each reaction's progression is governed by an equilibrium constant dependent on temperature, derived using Gibbs free energy principles. The expressions for the equilibrium constants are [48]:

$$K_1 = exp\left(\frac{\Delta G_1^0}{\overline{R}\ T_g}\right) = \left(\frac{n_5}{n_1^2}\right)\left(\frac{P}{n_{tot} \times P_0}\right)^{-1} \tag{8}$$

$$K_2 = exp\left(-\frac{\Delta G_2^0}{\overline{R}\ T_g}\right) = \left(\frac{n_1 \times n_3}{n_2 \times n_4}\right)\left(\frac{P}{n_{tot} \times P_0}\right)^{0} \tag{9}$$

where ΔG^0 refers to the standard Gibbs free energy change, R is the universal gas constant, T_g is the gasifier operating temperature, P is the system pressure, and P_0 is the reference pressure.

To calculate ΔG^0, the standard enthalpies and entropies of involved species are employed as follows [48]:

$$\Delta G_1^0 = \left(h_{CH_4} - T_g\ s^0_{CH_4}\right) - 2\left(h_{H_2} - T_g\ s^0_{H_2}\right) \tag{10}$$

$$\Delta G_2^0 = \left(h_{CO_2} - T_g\ s^0_{CO_2}\right) + \left(h_{H_2} - T_g\ s^0_{H_2}\right) - \left(h_{CO} - T_g\ s^0_{CO}\right) - \left(h_{H_2O} - T_g\ s^0_{H_2O}\right) \tag{11}$$

The energy balance within the gasifier is established by equating the total enthalpy of products with the total enthalpy of all reactants [48]:

$$\begin{aligned} \overline{h}^0_{f,\ \text{biomass}} + \ w \times \overline{h}^0_{f,H_2O} + m \times \overline{h}_{\text{air}} &= n_1\left(\overline{h}^0_{f,H_2} + \Delta\overline{h}_{H_2}\right) \\ +n_2\left(\overline{h}^0_{f,CO} + \Delta\overline{h}_{CO}\right) &+ n_3\left(\overline{h}^0_{f,CO_2} + \Delta\overline{h}_{CO_2}\right) \\ +n_4\left(\overline{h}^0_{f,H_2O} + \Delta\overline{h}_{H_2O}\right) &+ n_5\left(\overline{h}^0_{f,CH_4} + \Delta\overline{h}_{CH_4}\right) \\ &+ n_6\left(\overline{h}^0_{f,\ N_2} + \Delta\overline{h}_{N_2}\right) \end{aligned} \tag{12}$$

where $\overline{h}^0_f$ is the formations standard enthalpy, and $\Delta\overline{h}$ denotes the enthalpy change between reference and operating conditions for each species.

The lower heating value (LHV) is multiplied by a chemical exergy factor β to evaluate the chemical exergy of input biomass, where this factor is determined by the fuel's elemental composition [22]:

$$ex^{ch}_{\text{biomass}} = \beta \times LHV_{\text{biomass}} \tag{13}$$

The factor β is obtained using the empirical Szargut expression [22]:

$$\beta = \frac{1.044 + 0.0177\frac{H}{C} - 0.3328\frac{O}{C}\left(1 + 1.0537\frac{H}{C}\right)}{1 - 0.4021\frac{O}{C}} \tag{14}$$

where C, O, and H indicate mass fractions for carbon, oxygen, and hydrogen in the biomass feedstock.

3.2.2. PEM electrolysis

In the developed energy system, a PEM electrolyzer produces hydrogen by electrochemically breaking down water into hydrogen and oxygen using electricity and heat. [50]. The overall electrochemical reaction for this process is given by [51]:

$$H_2O \rightarrow H_2 + \frac{1}{2}O_2 \tag{15}$$

This equation consists of two half-cell reactions. A process of oxidation occurs at the anode, producing oxygen molecules, protons, and electrons:

$$H_2O \rightarrow 2H^+ + 2e^- + \frac{1}{2}O_2 \tag{16}$$

Hydrogen ions recombine to produce hydrogen gas at the cathode, where they take electrons:

$$2H^+ + 2e^- \rightarrow H_2 \tag{17}$$

The total energy necessary for the process, denoted by ΔH, is composed of two components [22]:

$$\Delta H = \Delta G + T\Delta S \tag{18}$$

Assuming moderate current densities and minimal concentration losses, the voltage required by the cell can be modeled as the sum of the reversible potential, kinetic losses at the electrodes, and the internal resistance across the PEM membrane [22]:

$$V = V_0 + V_{act,a} + V_{act,c} + V_{oh} \tag{19}$$

The reversible cell voltage (V_0), influenced by temperature, is calculated using [50]:

$$V_0 = 1.229 - 8.5 \times 10^{-4}(T_{PEM} - 298) \tag{20}$$

The ohmic loss term (V_{oh}) accounts for voltage drop due to internal resistance and is expressed as [51]:

$$V_{oh} = JR_{PEM} \tag{21}$$

In this expression, J denotes current density, and R_{PEM} is the overall resistance of the membrane, which depends on the membrane's proton conductivity and its water content distribution. The resistance is computed as follows [52]:

$$R_{PEM} = \int_0^L \frac{dx}{\sigma_{PEM}[\lambda_x]} \tag{22}$$

here L denotes the membrane thickness.

The local conductivity σ_{PEM} is described as a function of the water content (λ_x) and operating temperature [52]:

$$\sigma_{PEM} = (0.5139\lambda_x - 0.326)exp\left[1268\left(\frac{1}{303} - \frac{1}{T}\right)\right] \tag{23}$$

To determine λ_x across the membrane, a linear interpolation is used between the anode-side water content (λ_a) and the cathode-side value (λ_c) [53]:

$$\lambda_x = \frac{\lambda_a - \lambda_c}{Dm}x + \lambda_c \tag{24}$$

The activation overpotentials for both electrodes are calculated using a modified form of the Butler–Volmer equation, which involves the inverse hyperbolic sine function [22,51]:

$$\begin{cases} V_{act,a} = \dfrac{RT}{Fa} \times sinh^{-1}\left(\dfrac{J}{2J_{0,a}}\right) \\ V_{act,c} = \dfrac{RT}{Fa} \times sinh^{-1}\left(\dfrac{J}{2J_{0,c}}\right) \end{cases} \tag{25}$$

The exchange current densities ($J_{0,a}$ and $J_{0,c}$) are temperature-dependent and modeled using Arrhenius-type expressions [22]:

$$\begin{cases} J_{0,a} = J_a^{ref} \times exp\left(-\dfrac{E_{act,a}}{RT}\right) \\ J_{0,c} = J_c^{ref} \times exp\left(-\dfrac{E_{act,c}}{RT}\right) \end{cases} \tag{26}$$

where J_a^{ref} and J_c^{ref} are the respective reference values, and $E_{act,a}$, $E_{act,c}$ denote the activation energy at the anode and cathode.

Moreover, the productions rate of oxygen/hydrogen are calculated based on Faraday's law [22,51]:

$$\dot{N}_{O2} = \frac{J}{4Fa} \tag{27}$$

$$\dot{N}_{H2} = \frac{J}{2Fa} \tag{28}$$

3.2.3. Ammonia reactor

In the proposed process configuration, ammonia is produced through the catalytic combination of nitrogen and hydrogen using the Haber–Bosch synthesis route. The ammonia synthesis unit is modeled as a one-dimensional plug-flow reactor loaded with an iron-based catalyst, consistent with standard industrial practice. Nitrogen from the air separation unit is mixed with hydrogen under elevated temperature and pressure to achieve the desired reaction conditions. The feed composition is adjusted to maintain the stoichiometric molar ratio necessary for ammonia formation, corresponding to the hydrogen production rate from the upstream electrolyzer.

The overall reaction in the catalytic bed is represented as:

$$N_2(g) + 3H_2(g) \overset{Fe}{\rightleftarrows} 2NH_3(g) \Delta H = -92.4 \text{ kJ/mol} \tag{29}$$

Given the strongly exothermic nature of ammonia synthesis, both kinetic and thermodynamic effects must be accurately captured. In this study, the reaction rate is described using the Temkin–Pyzhev kinetic model, which differentiates the contributions of the forward and reverse reactions to account for non-ideal behavior. Accordingly, the net ammonia formation rate is expressed as [54]:

$$r_{NH_3} = r_{\text{forward}} - r_{\text{backward}} = k_1 \frac{P_{N_2} P_{H_2}^{1.5}}{P_{N_3}} - k_{-1} \frac{P_{N_3}}{P_{H_2}^{1.5}} \tag{30}$$

where the forward and reverse rates are functions of the partial pressures of nitrogen, hydrogen, and ammonia. The rate constants for both directions are evaluated using the Arrhenius expression [54]:

$$k = Ae^{\frac{-E_a}{RT}} \tag{31}$$

The kinetic parameters employed in this study are summarized in Table 2.

The Temkin–Pyzhev model effectively captures the influence of operating conditions on ammonia synthesis. Due to the exothermic nature of the reaction, temperature has a dual effect: it accelerates the intrinsic reaction rate via the Arrhenius dependence, while simultaneously shifting the equilibrium toward the reactants. In contrast, higher pressures favor ammonia production, as the reaction consumes a greater number of gas molecules. The dependence of the reaction rate on the partial pressures of reactants and products also reflects adsorption–desorption phenomena on the catalyst surface. By integrating both kinetic and thermodynamic considerations, this model provides a realistic prediction of ammonia synthesis performance across a range of temperatures, pressures, and feed compositions.

3.3. Thermodynamic modeling

The conservation of mass within each component can be described by the following general expression [56,57]:

$$\sum_i \dot{m}_i = \sum_e \dot{m}_e \tag{32}$$

For energy conservation, the first law of thermodynamics is applied to the components as:

$$\dot{Q} - \dot{W} = \sum_e \dot{m}_e h_e - \sum_i \dot{m}_i h_i \tag{33}$$

To evaluate system performance from a second-law standpoint, the exergy balance across a control volume is written as [49]:

Table 2
Temkin–Pyzhev kinetic parameters used for ammonia synthesis [54,55].

Parameter	$E_a(kJ/kg{\cdot}mol)$	$A(-)$
k_1	87,027	17,895
k_2	1.9832×10^5	2.5714×10^{16}

$$\dot{E}x_Q + \sum_i \dot{m}_i ex_i = \sum_e \dot{m}_e ex_e + \dot{E}x_W + \dot{E}x_d \tag{34}$$

The exergy transfer via heat at a given temperature T is defined as [58]:

$$\dot{E}x_Q = \left(1 - \frac{T_0}{T}\right)\dot{Q} \tag{35}$$

The work-related exergy component is directly equivalent to the work rate:

$$\dot{E}x_W = \dot{W} \tag{36}$$

Physical and chemical exergy make up the total energy carried by each flow stream in the system [59]:

$$ex_i = ex_{ch,i} + ex_{ph,i} \tag{37}$$

The physical exergy, representing deviation from the environmental reference state, is calculated as [57]:

$$ex_{ph} = (h - h_0) - T_0(s - s_0) \tag{38}$$

For chemical exergy of gas mixtures undergoing reactions, the expression is [59]:

$$ex_{ch,gasmixture} = \sum x_i ex_{ch,i}^0 + RT_0 \sum x_i \ln(x_i) \tag{39}$$

In this equation, x_i is the mole fraction of component i within the mixture, and $ex_{ch,i}^0$ represents its standard chemical exergy.

Based on the integrated configuration, the power generation is calculated as the sum of the contributions from the different generation units:

$$\dot{W}_{Generation} = \dot{W}_{AT} + \dot{W}_{GT} + \dot{W}_{Turb1} + \dot{W}_{Turb2} \tag{40}$$

Similarly, the total power consumption is given by:

$$\dot{W}_{Generation} = \dot{W}_{sCO2} + \dot{W}_{Electrical} + \sum_{k=1}^{7} \dot{W}_{Comp,k} + \dot{W}_{PEM} \tag{41}$$

In this configuration, seven compressors are considered: three air compressors, the MC and RC of the S-CO_2 cycle, and the hydrogen and nitrogen compressors. Here, $\dot{W}_{PEM}$ represents the electrical power delivered to the PEM electrolyzer, which is supplied by 85% of the power generated from the S-CO_2/geothermal sections. The term $\dot{W}_{Electrical}$ accounts for the electrical work required for nitrogen production via air separation, which is provided by the remaining S-CO_2/geothermal power and, if needed, by the GT section. The electrical energy demand for air separation is assumed to be 0.25 kWh per kg of N_2 produced.

3.3.1. Supercritical CO_2 cycle

The S-CO_2 recompression Brayton cycle is employed in this investigation to harness the high-grade thermal energy of the flue gas, leveraging CO_2's supercritical properties to enhance thermal efficiency and optimize energy recovery. A set of governing equations derived from the first law and second law of thermodynamics are employed to determine the mass flow rate and thermodynamic state properties at each point in the cycle. These relationships are systematically applied across the entire cycle, ensuring that both the inlet and outlet energy flows are balanced for each device.

For the modeling of the recompression cycle, the split ratio (SR) denotes the proportion of the total working fluid mass flow directed into the MC. It is mathematically defined as:

$$SR = \frac{\dot{m}_{MC}}{\dot{m}_{CO2}} \tag{42}$$

Fig. 3 illustrates the computational workflow adopted for simulating

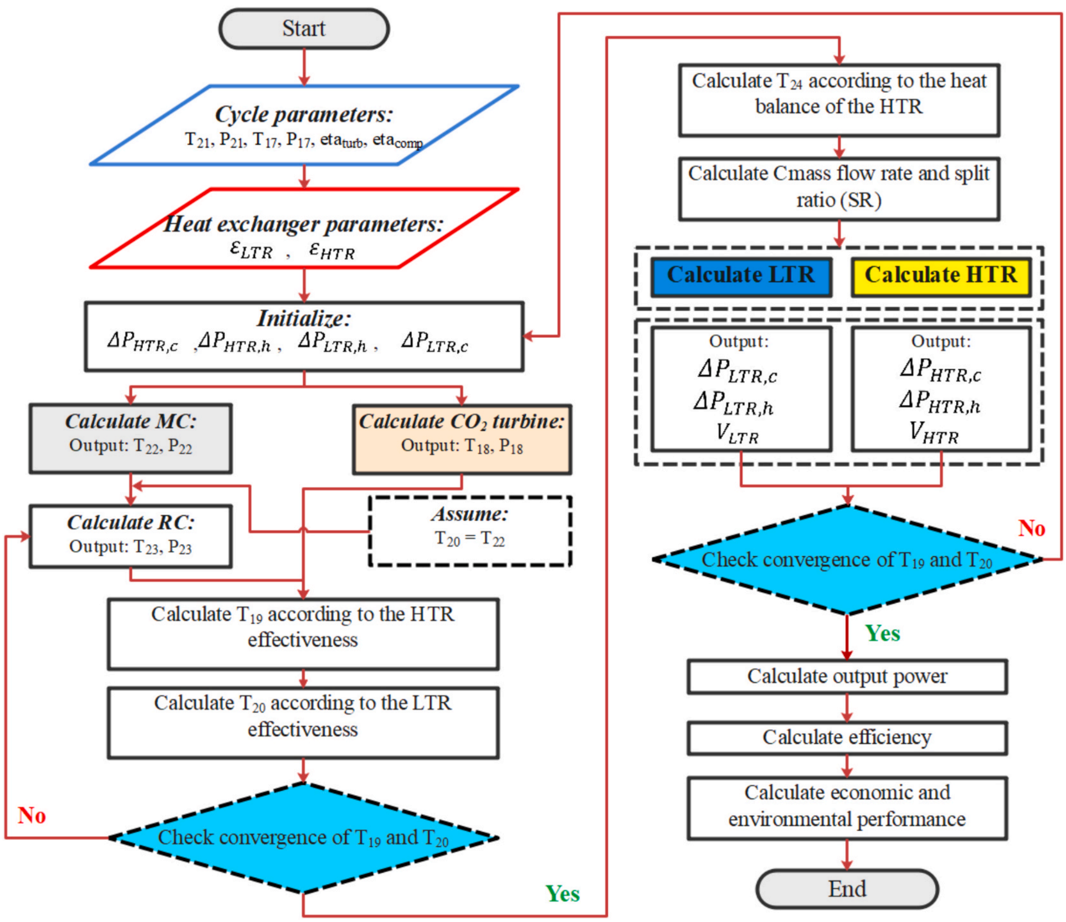

Fig. 3. Computational flow diagram for S-CO_2 recompression Brayton cycle simulation.

Table 3
S-CO_2 Brayton cycle key design and thermodynamic input parameters.

Parameters	Value
MC inlet temperature (K)	308
MC inlet pressure (MPa)	10
Turbine inlet temperature (K)	865
Turbine inlet pressure (MPa)	20
Cooling water inlet temperature	298
Split ratio	0.7
Turbine isentropic efficiency	0.9
Compressor isentropic efficiency	0.85

the recompression S-CO_2 Brayton cycle. This process begins by introducing the primary thermodynamic and design parameters listed in Table 3. Pressure losses across components are assumed to remain constant. A zero-dimensional modeling approach is applied to initialize the cycle boundaries and estimate the initial state conditions.

Assuming thermal equality between state points 20 and 22, performance calculations are carried out for the MC, RC, and turbine, yielding updated values for states 18, 22, and 23. Based on the specified effectiveness values, outlet temperatures at states 19 and 20 are computed through energy balance in the recuperators. An iterative loop is executed to achieve convergence of states 19 and 20. Once the values stabilize, the energy balance in the HTR is used to determine the conditions at state 24. At this stage, the mass flow distribution and recompression SR are also calculated. Finally, system-level metrics such as net output power, overall cycle efficiency, and environmental and economic performance indicators are evaluated.

3.4. Exergoeconomic and environmental analysis

To comprehensively evaluate the proposed framework's performance, it is important to evaluate not only thermodynamic behavior but also financial viability and environmental implications. This section outlines the methodology used to quantify the cost associated with exergy flows and the environmental impact resulting from fuel consumption and component inefficiencies. By coupling exergy analysis with economic and emission metrics, a deeper insight into system sustainability and optimization potential is achieved.

The exergoeconomic formulation for each component k is mathematically described as [22]:

$$\sum \dot{C}_{e,k} + \dot{C}_{w,k} = \sum \dot{C}_{i,k} + \dot{C}_{Q,k} + \dot{Z}_k \tag{43}$$

Each individual cost term $\dot{C}$ is determined using the respective exergy flow rate $\dot{E}_x$ and specific cost of the exergy (c) [60]:

$$\dot{C} = c \times \dot{E}_x \tag{44}$$

The term $\dot{Z}_k$ accounts for the annualized cost of capital investment and maintenance for component k, and is evaluated using the expression [61]:

$$\dot{Z}_k = \frac{CRF \times \phi}{\tau \times 3600} Z_k \tag{45}$$

here ϕ denotes the maintenance factor, and τ denotes the annual running hours, and Z_k denotes the element's acquisition cost. In order to spread the initial financial investment across the anticipated life service of a system, capital recovery factor (CRF) is calculated as follows [62,63]:

$$CRF = \frac{i(1+i)^n}{(1+i)^n - 1} \tag{46}$$

In this equation n denotes the system's economic life in years, and i indicates the annual interest rate. The financial parameters utilized in the exergoeconomic analysis of this study are presented in Table 4.

To align older cost data with current financial conditions, a cost correction factor based on cost indices is applied. The present value of the component cost is determined using [57,66]:

$$\dot{Z}_{\text{Present}} = \dot{Z}_{Reference} \times \frac{CI_{Present}}{CI_{Reference}} \tag{47}$$

where $\dot{Z}_{Reference}$ is the historical component cost, and $CI_{Reference}$ and $CI_{Present}$ refer to the cost indices of the reference and current years, respectively.

The cost estimation equations for primary components used in the system's exergoeconomic evaluation—derived from supplier quotes, empirical models, or published sources—are presented in Table 5. These correlations are typically expressed as functions of design characteristics such as thermal duty, electrical output, or heat transfer surface area.

The levelized cost of electricity (LCOE) is used to evaluate the economic performance of the suggested platform in producing electrical power. This indicator represents the average cost per unit of net electricity generated over the operational lifetime of the plant. In this study, the LCOE is calculated by considering the annualized capital cost rates of the components directly involved in the electricity generation process. These components include the gas turbine cycle, the S-CO_2 Brayton cycle, and the geothermal power generation unit. Since the hydrogen production and ammonia synthesis units constitute a secondary product pathway and are not part of the electricity generation chain, their associated costs are not included in the LCOE calculation. Therefore, the LCOE represents the cost per unit of electricity produced by the electricity-generating subsystems of the integrated plant. It is calculated by dividing the total annualized capital costs of all electricity-generating components by the net annual electricity output, as shown in the following expression [59].

$$LCOE = \frac{\dot{Z}_{GTC} + \dot{Z}_{S-CO2} + \dot{Z}_{Geo}}{\dot{W}_{\text{net}}} \tag{48}$$

where $\dot{Z}_{GTC}$ presents the cost rate of the air compressors, gasifier, intercooler, air/gas turbines, and preheater. $\dot{Z}_{S-CO2}$, and $\dot{Z}_{Geo}$ represent the cost rates of all components in the S-CO_2 cycle and the geothermal unit, respectively. Also, the system's total net electrical power generated is denoted by $\dot{W}_{net}$.

The levelized cost of ammonia (LCOA) is calculated as:

$$LCOA = \frac{\dot{Z}_{Ammonia} + (\dot{W}_{Consumption} \times LCOE)}{M_{Ammonia}} \tag{49}$$

where $\dot{Z}_{Ammonia}$ represents the total cost rate associated with the components directly involved in the ammonia production section, including the PEM electrolyzer, PEM preheater, separator, hydrogen storage tank, hydrogen compressor, nitrogen compressor, and ammonia synthesis reactor. $\dot{W}_{Consumption}$ denotes the total electrical power consumed by the ammonia production subsystem, primarily by the electrolyzer and compressors. The cost of the consumed electricity is calculated using the LCOE obtained for the overall system.

Table 4
Input values for economic investigation [64,65].

Parameter	Value
Annual operational duration (T)	8000 h
Lifetime (N)	20 years
Rate of interest (i)	12%
Operation and maintenance component (Φ)	1.06

The net present value (NPV) is another crucial indicator used to assess the system's financial performance. It integrates both expenditures and revenues across the project's operational lifespan and is determined using the following expression [67,68]:

$$NPV = -TFC + \sum_{i=1}^{n} (AMS \times IF_i \times RDF_i) \tag{50}$$

where the TFC is composed of direct costs (DC) and indirect costs (IC):

$$TFC = DC + IC \tag{51}$$

The annual monetary savings (AMS) are calculated as [69,70]:

$$AMS = AI - 0.06 \times FC \tag{52}$$

To account for economic fluctuations over time, two correction coefficients are applied: the inflation factor (IF_i) and the real discount factor (RDF_i), which can be computed as [71]:

$$IF_i = \left(1 + \frac{R}{100}\right)^{-i} \tag{53}$$

$$RDF_i = \left(1 + \frac{RIR}{100}\right)^{-i} \tag{54}$$

The minimal number of years needed for the cumulative NPV to reach zero or positive, signifying that the initial capital expenditure has been completely recovered, is known as the payback period (PP):

$$PP = n, ifNPV = 0 \tag{55}$$

The environmental impact of the plant is evaluated using the carbon dioxide emission index, given the significant role of CO_2 as a leading greenhouse gas associated with global warming, particularly from energy generation processes. This index measures the mass of carbon dioxide emitted per unit of useful energy output produced by the system. For a hybrid facility that simultaneously produces electricity and ammonia, the emission index can be expressed as [72]:

$$\zeta_{\text{emission}} = \frac{\dot{m}_{CO2}}{\dot{E}_{\text{Product}}} = \frac{\dot{m}_{CO2}}{\dot{W}_{\text{net}} + \dot{E}_{NH_3}} \tag{56}$$

where $\dot{m}_{CO2}$ denotes the CO_2 emission rate, $\dot{W}_{\text{net}}$ is the net power output, and $\dot{E}_{NH_3}$ represents the energy content associated with ammonia production.

In addition, the sustainability index (SI) is introduced as an indicator to gauge how improvements in energy efficiency contribute to environmental protection. It is described as the depletion factor's (DP) inverse [40]:

$$SI = \frac{1}{D_P} \tag{57}$$

The depletion factor measures how much of the exergy within the system is lost compared with the exergy that is input, and is calculated as:

$$D_P = \frac{\sum_{k=1}^{n_k} \dot{E}_{D,k}}{\dot{E}_{in}} \tag{58}$$

4. Data-driven optimization

Data-driven methods leveraging artificial intelligence are playing an increasingly pivotal role in the energy sector, enabling advanced modeling and optimization of complex systems [73,74]. To improve the overall performance of the suggested framework, a comprehensive optimization study is conducted with the goal of simultaneously improving system efficiency and economic viability. This multi-objective optimization problem involves complex, nonlinear

Table 5
Cost models for the main components [22,30,40].

Component	Cost function ($)	$CI_{Reference}$
Air compressor	$Z_{Compressor} = 91562 \times (\dot{W}_{Comp.}/455)^{0.67}$	368
Gasifier	$Z_G = 1600 \times (\dot{m}_{\mathrm{biomass}})^{0.67}$	368
Combustion chamber	$Z_{CC} = \left(\frac{46.08 \times \dot{m}_{out}}{0.995 - P_{out}/P_{in}}\right)[-26.4 + exp(0.018 \times T_{comb.}) + 1]$	394.1
Gas turbine	$Z_{GT} = 479.34 \times \left(\frac{\dot{m}_{11}}{0.93 - \eta_{\mathrm{Turb}\ 1}}\right) ln\left(\frac{P_{11}}{P_{12}}\right) \times (exp(0.036 \times T_{11} - 54.4) + 1)$	368
Air turbine	$Z_{AT} = 479.34 \times \left(\frac{\dot{m}_{9}}{0.93 - \eta_{\mathrm{Turb}\ 1}}\right) ln\left(\frac{P_{9}}{P_{10}}\right) \times (exp(0.036 \times T_{9} - 54.4) + 1)$	368
Air preheater	$Z_{AP} = 4112\left(\frac{(h_{12} - h_{13})\dot{m}_{12}}{\Delta T_{lm,AP} U_{AP}}\right)^{0.6}$	368
Intercooler	$Z_{IC} = 8000\left(\frac{A_{IC}}{100}\right)^{0.6}$	394.1
CO_2 evaporator	$Z_{\mathrm{evap}} = 2143 \times (A_{evap}{}^{0.514})$	567.3
CO_2 turbine	$Z_{\mathrm{TSCO2}} = 479.34 \times \frac{\dot{m}_{\mathrm{in}}}{0.93 - \eta_{\mathrm{is\ ,\ TSC2}}} \times ln\left(\frac{p_{\mathrm{in}}}{p_{\mathrm{out}}}\right) \times (1 + exp(0.036 \times T_{\mathrm{in}} - 54.4))$	402.3
MC	$Z_{\mathrm{MC}} = 71.1 \times \frac{\dot{m}_{\mathrm{in}}}{0.92 - \eta_{\mathrm{is}\ ,MC}} \times \left(\frac{p_{\mathrm{out}}}{p_{\mathrm{in}}}\right) \times ln\left(\frac{p_{\mathrm{out}}}{p_{\mathrm{in}}}\right)$	368
RC	$Z_{\mathrm{RC}} = 71.1 \times \frac{\dot{m}_{\mathrm{in}}}{0.92 - \eta_{\mathrm{is\ ,\ RC}}} \times \left(\frac{p_{\mathrm{out}}}{p_{\mathrm{in}}}\right) \times ln\left(\frac{p_{\mathrm{out}}}{p_{\mathrm{in}}}\right)$	368
HTR	$Z_{\mathrm{HTR}} = 130\left(\frac{A_{\mathrm{HTR}}}{0.093}\right)^{0.78}$	468.2
LTR	$Z_{LTR} = 130\left(\frac{A_{LTR}}{0.093}\right)^{0.78}$	468.2
Cooler	$Z_{Cooler} = 2681(A_{Cooler})^{0.59}$	368
Turbine 1	$Z_{\mathrm{Tur1}} = 3880.5 \times \dot{W}_{\mathrm{Tur1}}^{0.7}\left(1 + \left(\frac{0.05}{0.92 - \eta_{\mathrm{is\ ,\ Tur1}}}\right)^3\right)\left(1 + 5 \times 2.71\frac{(T_{27} - 866)}{10.42}\right)$	402
Turbine 2	$Z_{\mathrm{Tur2}} = 3880.5 \times \dot{W}_{\mathrm{Tur2}}^{0.7}\left(1 + \left(\frac{0.05}{0.92 - \eta_{\mathrm{is\ ,\ Tur2}}}\right)^3\right)\left(1 + 5 \times 2.71\frac{(T_{29} - 866)}{10.42}\right)$	402
GHEX	$Z_{GHEX} = 2681(A_{GHEX})^{0.59}$	368
Mixer	$Z_{Mixer} = 50 \times \dot{m}_{mixer}$	499.6
Condenser	$Z_{Cond} = 130\left(\frac{A_{Cond}}{0.093}\right)^{0.78}$	468.2
Valve	$Z_V = 114.5 \times \dot{m}_V$	394.1
PEM electrolyzer	$Z_{PEME} = 1000 \times \dot{W}_{elec}$	603.1
Preheater	$Z_{Preheater} = 130\left(\frac{A_{Pre}}{0.093}\right)^{0.78}$	468.2
H_2 compressor	$71.1 \times \dot{m}_{43} \times \left(\frac{1}{0.92 - \eta_{\mathrm{is.com}}}\right) \times \left(\frac{P_{44}}{P_{43}}\right) \times Ln\left(\frac{P_{44}}{P_{43}}\right)$	468.2
N_2 compressor	$71.1 \times \dot{m}_{45} \times \left(\frac{1}{0.92 - \eta_{\mathrm{is.com}}}\right) \times \left(\frac{P_{46}}{P_{45}}\right) \times Ln\left(\frac{P_{46}}{P_{45}}\right)$	468.2
Ammonia reactor	$Z_{AR} = 610 \times \dot{W}_{Input}$	603.1

interactions among design parameters; therefore, a data-driven modeling and optimization strategy is employed to ensure both computational efficiency and accuracy.

4.1. Design parameters and objective functions

The optimization problem is formulated using five parameters, carefully selected due to their thermodynamic and operational significance. Table 6 presents the selected variables together with their corresponding bounds. The bounds of these variables were selected based on typical operating conditions reported in previous studies as well as engineering limitations associated with the system components. In particular, the inlet pressures of the geothermal turbines were restricted to ranges that allow stable expansion within the dual-flash geothermal configuration. The geothermal fluid temperature range was selected to represent typical medium- to high-temperature geothermal reservoirs suitable for power generation. The gas turbine inlet temperature was bounded according to common operational limits of gas turbines fueled by biomass-derived syngas, considering turbine material limitations and thermal stability. Furthermore, the split ratio of the supercritical carbon dioxide Brayton cycle was limited to a practical range to ensure proper flow distribution and stable cycle performance.

The three objective functions include the maximization of exergy efficiency (EE), which enhances the thermodynamic efficiency of the framework; the maximization of ammonia production rate (APR), reflecting the capacity for chemical output; and the minimization of the LCOE, to ensure overall economic feasibility.

Table 6
The decision variables and their operational ranges.

Decision variable	Symbol	Lower bound	Upper bound	Unit
Inlet pressure of Turbine 1	P_{27}	200	600	kPa
Inlet pressure of Turbine 2	P_{29}	20	80	kPa
Geothermal fluid temperature	$T_{Geofluid}$	190	250	°C
Gas turbine inlet temperature	$GTIT$	925	1325	°C
S-CO_2 split ratio	SR	0.55	0.85	–

4.2. Data preparation and ANN modeling

A total of 3200 datasets are generated using random sampling of the decision space within the defined bounds. Each data point corresponds to a full simulation run, from which EE, APR, and LCOE are extracted. To approximate the system behavior, three distinct ANNs are trained, each representing one function. The datasets are split into 75% training, 15% validation, and 10% testing subsets [75]. The network architecture and performance metrics are shown in Table 7.

Each trained ANN effectively replaces the full thermodynamic model

Table 7
ANN structure and predictive performance for each objective.

Objective	Hidden layers	Activation function	Neurons per layer	Performance metric
EE	2	Tansig–Purelin	[8,10]	MSE,R^2
APR	2	Tansig–Purelin	[10,12]	MSE,R^2
LCOE	2	Tansig–Purelin	[10,12]	MSE,R^2

during optimization, significantly reducing computational time. The general workflow of data generation, training, and integration into optimization is illustrated in Fig. 4.

4.3. Multi-objective optimization with MOPSO

The multi-objective particle swarm optimization (MOPSO) method is used to solve the tri-objective problem. MOPSO is selected for its superior convergence characteristics and ability to maintain a diverse Pareto front. The trained ANN models serve as fast surrogate evaluators for EE, APR, and LCOE within the MOPSO framework. The algorithm explores the decision space through swarm dynamics and elitism mechanisms to identify a set of Pareto-optimal solutions. Fig. 5 depicts the MOPSO algorithm's operational flowchart. providing a clear representation of the iterative search mechanism and integration of surrogate models.

4.4. Decision-making approach

A multi-criteria decision-making (MCDM) strategy is needed to select a fair compromise among the conflicting objectives after the Pareto front has been established. For this purpose, the LINMAP method is employed.

First, all objective values are normalized using the following formula:

$$f_{i,j}^{*} = \frac{f_{i,j}}{\sqrt{\sum_{i=1}^{N} (f_{i,j})^2}}, j = 1, 2, 3 \tag{59}$$

The ideal point in normalized space is determined as [59]:

$$f_{ideal,j}^{*} = minf_{i,j}, j = 1, 2, 3 \tag{60}$$

The Euclidean distance between this ideal point and every Pareto solution is calculated [59]:

$$d_i = \sqrt{\sum_{j=1}^{3} \left(f_{i,j}^{*} - f_{ideal,j}^{*}\right)^2} \tag{61}$$

The most effective choice is the design point that has the least amount of distance, signifying a well-balanced trade-off among EE, APR, and LCOE.

5. Validation

A rigorous validation process was undertaken to show the accuracy and dependability of the developed simulation models for the proposed multigeneration unit. This involved comparing key subsystem outputs with results from published experimental or simulation-based studies, as well as evaluating the fidelity of the trained ANNs used in the optimization process.

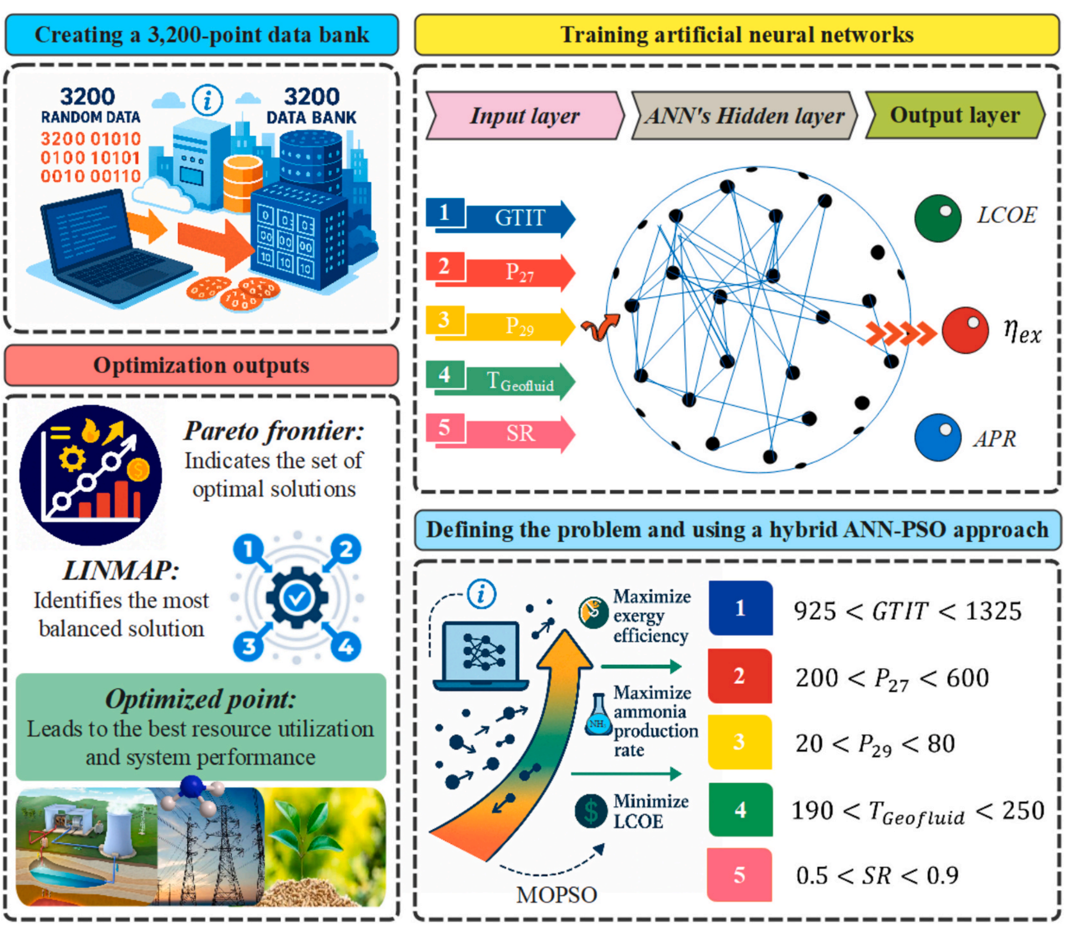

Fig. 4. Schematic workflow of the data-driven multi-objective optimization procedure.

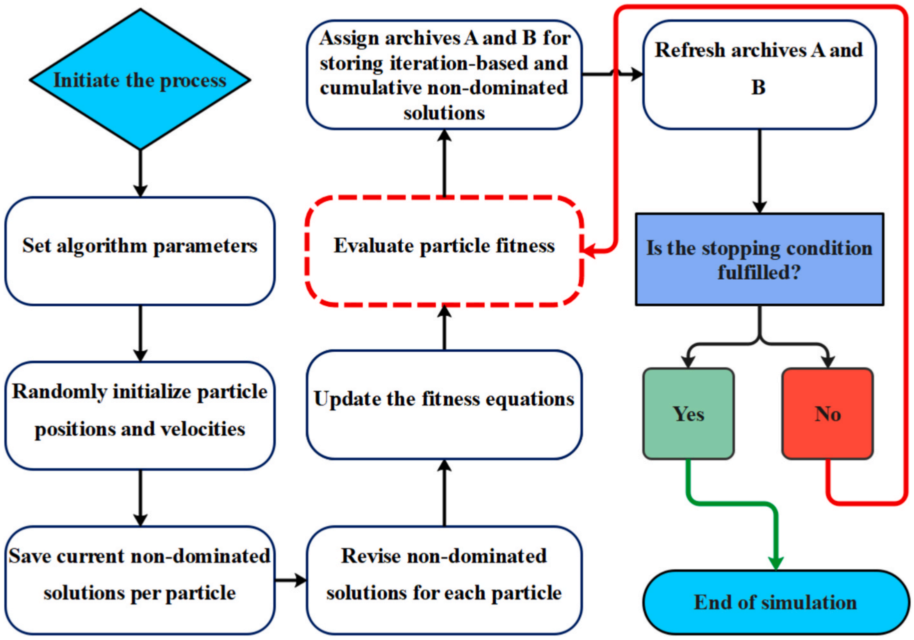

Fig. 5. Flowchart of the MOPSO algorithm used for the tri-objective optimization.

5.1. *Subsystem validation*

To validate the electrochemical model of the PEM electrolyzer, simulation data were compared with the experimental data provided by Ioroi et al. [76]. Fig. 6 demonstrates a close agreement between the modeled polarization behavior and the reference data across the operating voltage range. Model validation for ammonia synthesis was conducted by comparison with the experimental data reported by Lundgren et al. [77], as presented in Fig. 7. The observed deviations are within acceptable engineering limits, confirming the accuracy and robustness of the Temkin–Pyzhev kinetic model and the plug-flow reactor representation. Moreover, the gasification model was validated through the comparison of the simulated syngas composition with the experimental results presented by Zainal et al. [78] and Alauddin [79]. As shown in Fig. 8, the predicted volumetric fractions of major components—CO, H_2, CH_4, and CO_2—closely match the referenced values.

Further, the S-CO2 Brayton cycle's performance was validated against the reported simulation data from Wu et al. [80]. Table 8 presents a detailed comparison of key thermodynamic parameters, including turbine output, compressor work, and net power generation. The deviations between the present model and the literature data

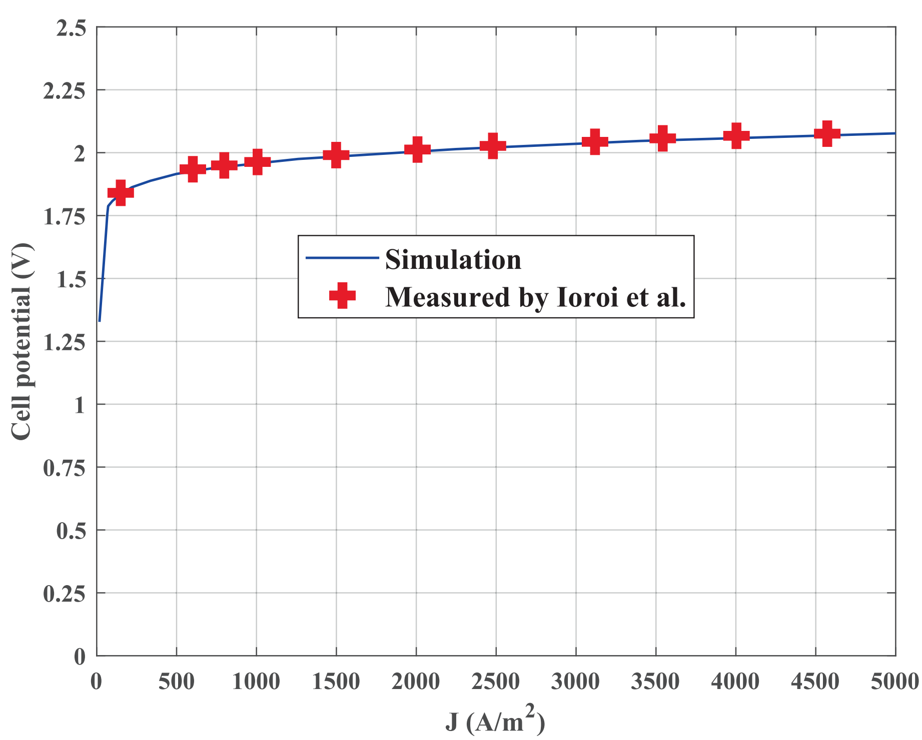

Fig. 6. Validation of the PEM electrolyzer model by comparison with experimental polarization data from Ioroi et al. [76].

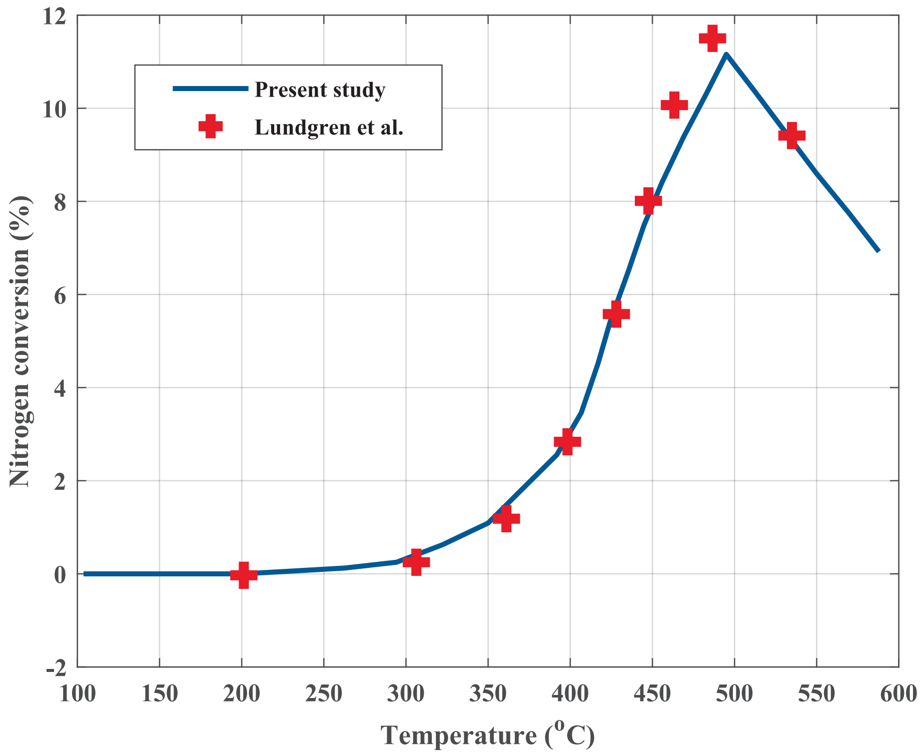

Fig. 7. Comparison of simulated ammonia synthesis performance with literature data [77] for model validation.

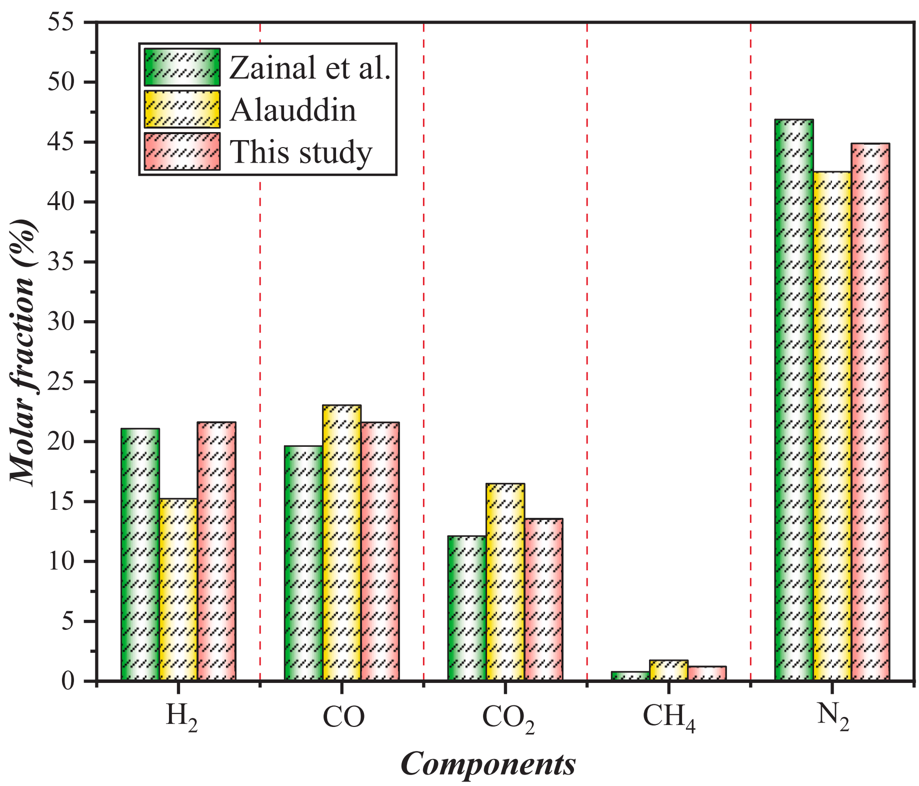

Fig. 8. Comparison of simulated syngas composition from the model with experimental data presented by Zainal et al. [78] and Alauddin [79].

Table 8
Validation of the S–CO_2 recompression Brayton cycle.

Parameter	Wu et al. [80]	Simulation	Error (%)
$\dot{W}_{RC}$(MW)	73.53	73.42	0.14
$\dot{W}_{Tur}$(MW)	393.2	393.34	0.03
$\dot{W}_{MC}$(MW)	76.09	76.37	0.37
$\dot{Q}_{LTR}$(MW)	463.36	463.49	0.03
$\dot{Q}_{HTR}$(MW)	571.40	571.09	0.05

remain below 0.4% for all parameters, demonstrating high consistency and accuracy of the implemented S-CO_2 cycle model.

5.2. ANN model validation

In addition to system validations, the predictive capabilities of the trained ANNs—used as surrogate models during multi-objective optimization—were also assessed. During model validation, the coefficient of determination (R^2) was applied as a statistical metric to evaluate predictive accuracy, indicating how much of the variability in the target variables is accounted for by the model's predictions [81]. Fig. 9 illustrates the regression performance of the ANNs for all three objective functions. The results show high R^2 values and minimal mean squared errors (MSE), confirming that the neural networks effectively represented the nonlinear associations between decision factors and target outputs.

6. Results and discussion

The following section provides an in-depth investigation of the proposed multigeneration framework from economic, thermodynamic, and optimization viewpoints. First, the base-case performance is evaluated. Subsequently, results from the data-driven multi-objective optimization are discussed, highlighting the trade-offs among thermodynamic performance, production capacity, and economic feasibility. Finally, a detailed economic investigation is conducted to determine the system's long-term viability.

To initiate the analysis, the key input parameters used for simulating the base system configuration are summarized in Table 9. It is worth noting that the specific input data related to the S-CO_2 cycle were previously presented in Table 3.

6.1. Exergy-based results

Fig. 10 shows a comprehensive exergy destructions analysis of the proposed integrated multigeneration framework. The diagram not only highlights the contribution of each primary subsystem to the total irreversibility but also drills down into component-level inefficiencies within each unit.

As observed in Fig. 10, the predominant contributor to exergy destruction is the gas turbine-based subsystem, responsible for approximately 70.6% of the total system irreversibility (4148.95 kW). This high value is largely attributed to the combustion process, which inherently involves significant thermodynamic irreversibility due to the large

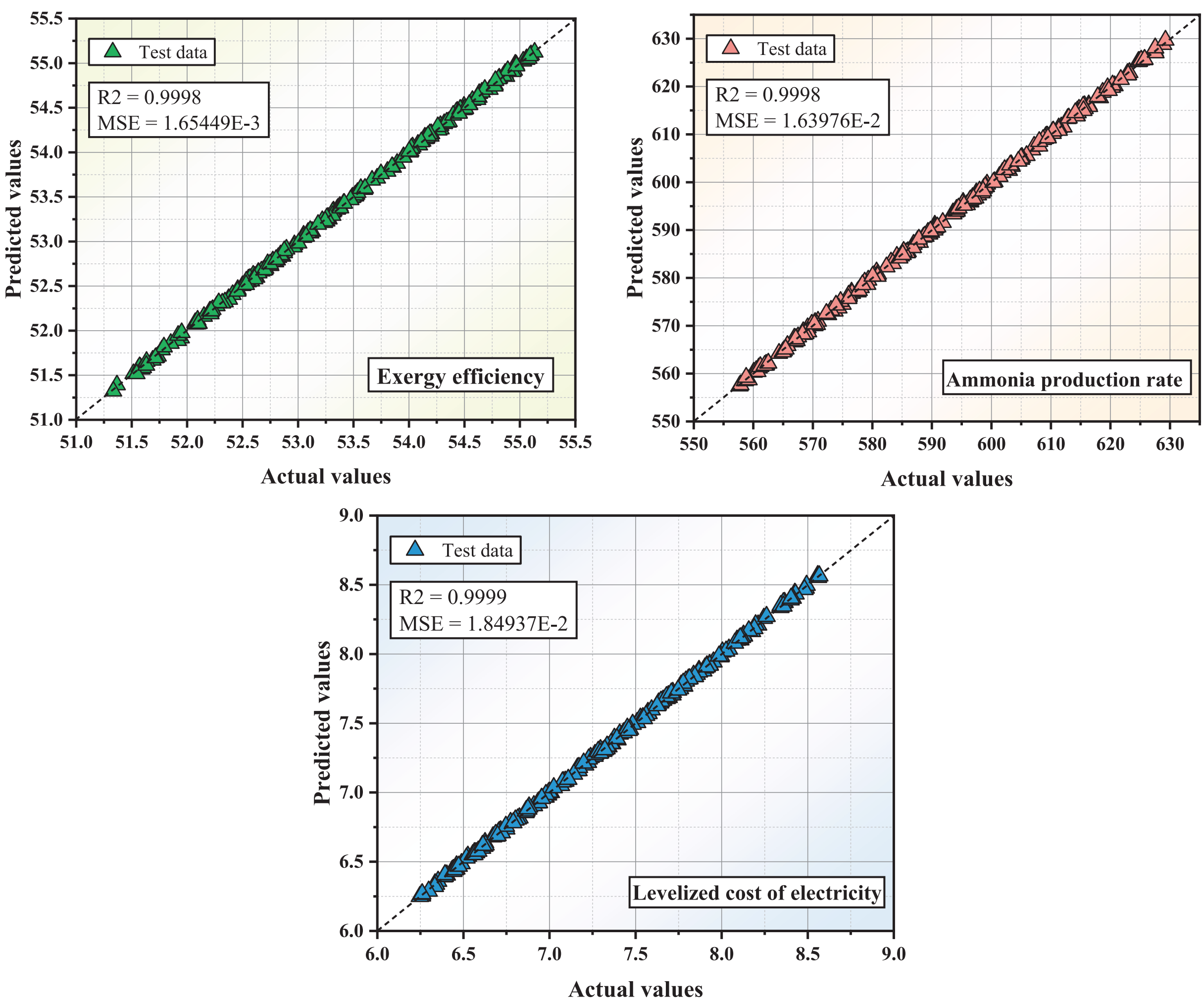

Fig. 9. Regression plots for the trained ANNs predicting EE, APR, and LCOE.

Table 9
Input parameters used for system analysis [30,40,82].

Parameter	Value	Unit
Gasification pressure	400	kPa
Gasification temperature	800	°C
Compressor 1 pressure ratio	14	–
Compressor 2 pressure ratio	5	–
Pumps isentropic efficiency	90	%
Compressors isentropic efficiency	85	%
Gas turbines isentropic efficiency	86	%
Steam turbine isentropic efficiency	88	%
Temperature of inlet geothermal fluid	230	°C
Mass flow rate of geothermal fluid	10	Kg/s
Inlet pressure of FC 2	500	kPa
Inlet pressure of FC 2	70	kPa
Electrolyzer cell temperature during operation	80	°C
Discharge pressure of produced hydrogen	101.3	kPa
Exchange current density at anode	2×10^5	A/m^2
Exchange current density at cathode	4.6×10^3	A/m^2
Activation energy at cathode	18	kJ/mol
Activation energy at anode	76	kJ/mol
Oxygen outlet pressure	101.3	kPa
Thickness of the PEM layer	50	μm
λ_a	14	–
λ_c	10	–
Temperature of hydrogen after compression	250	°C
Final pressure of compressed hydrogen	10,000	kPa
Temperature of nitrogen after compression stage	250	°C
Discharge pressure of compressed nitrogen stream	10,000	kPa
Synthesis pressure of ammonia	10,000	kPa
Synthesis temperature of ammonia	250	°C

temperature gradients and the generation of entropy during fuel oxidation. Specifically, the CC alone contributes 1844.57 kW, making it the single most inefficient component in the system. The gasifier, which converts biomass into syngas, is another key contributor (1129.71 kW) due to the complex reactions involved and the challenge of maintaining equilibrium conditions. Additional losses stem from the AP (491.71 kW) and IC (241.89 kW), both of which are involved in thermal exchange processes that are subject to temperature mismatches and imperfect heat recovery. Compressors and turbines, while necessary for cycle operation, also introduce notable exergy losses due to non-ideal compression and expansion, as seen in Comp. 1–3 and AT.

The geothermal subsystem accounts for 20.2% of total exergy destruction (1188.14 kW). The geothermal expansion valve (GEV) and condenser are the primary sources of irreversibility, contributing 241.8 kW and 239.4 kW, respectively. The GEV suffers from throttling losses due to pressure drops without energy recovery, while the condenser represents a major site of exergy loss due to heat rejection to the environment. Turbines 1 and 2 also contribute (90.52 kW and 146.7 kW) due to the inherent inefficiencies in expanding low-enthalpy geothermal fluid. Geothermal heat exchangers (GHEX 1 and 2) also exhibit considerable irreversibility (totaling 268.32 kW), attributed to finite temperature differences and imperfect thermal contact.

The S-CO_2 Brayton cycle, although relatively more efficient, still contributes 5.1% of the total exergy destruction (297.5 kW), as seen in Fig. 10. Here, the CO_2 turbine (60.2 kW) and cooler (66.15 kW) are the main contributors. The turbine losses are typical of expansion devices operating under real conditions with non-ideal isentropic performance. The cooler, responsible for rejecting waste heat, inherently incurs losses as it discharges thermal energy to the surroundings. The recuperators (HTR and LTR) also exhibit non-negligible exergy destruction (54.95 kW and 44.1 kW, respectively), primarily due to thermal mismatches and effectiveness limitations. Compressors (MC and RC) and the CO_2

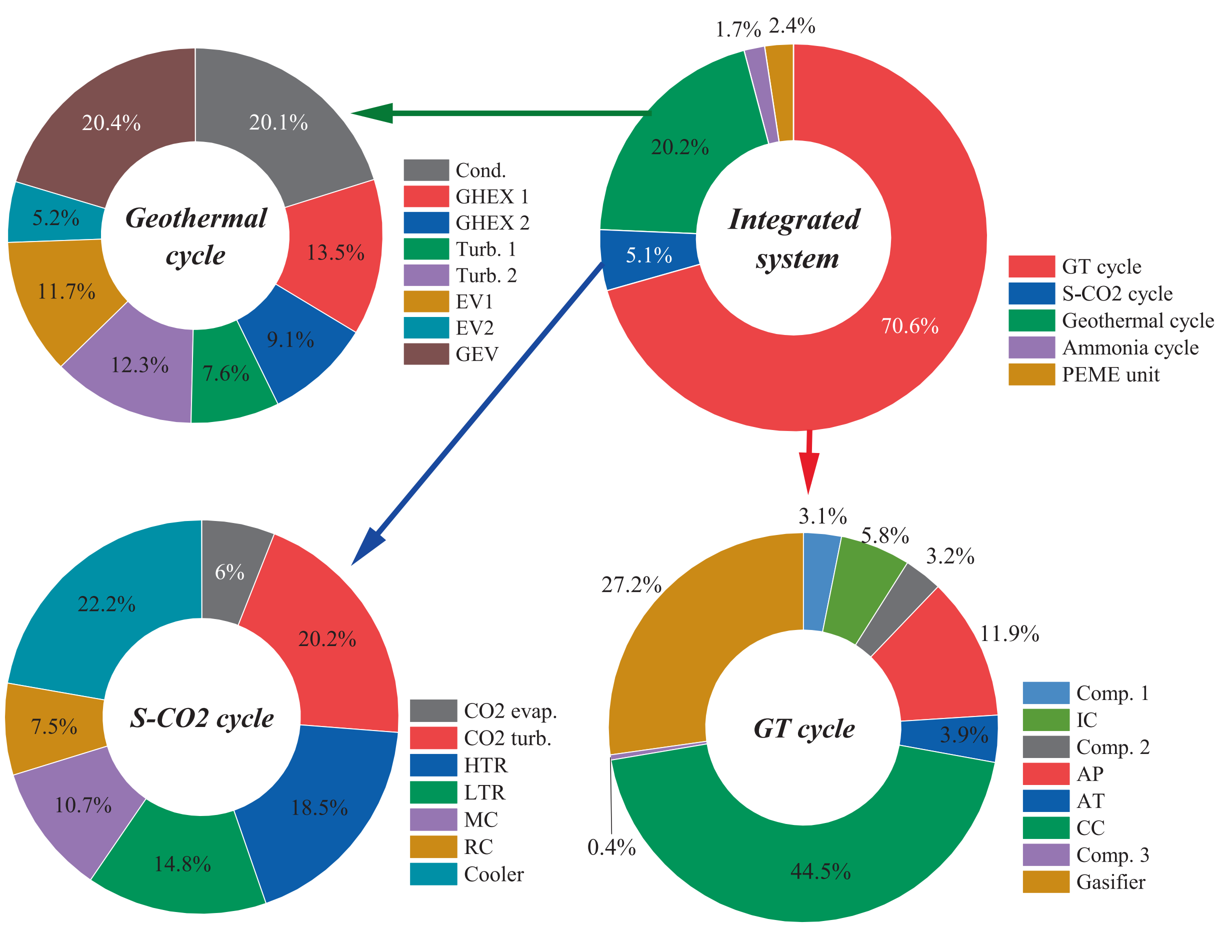

Fig. 10. Distribution of exergy destruction throughout the main internal elements and subsystems of the presented multigeneration system.

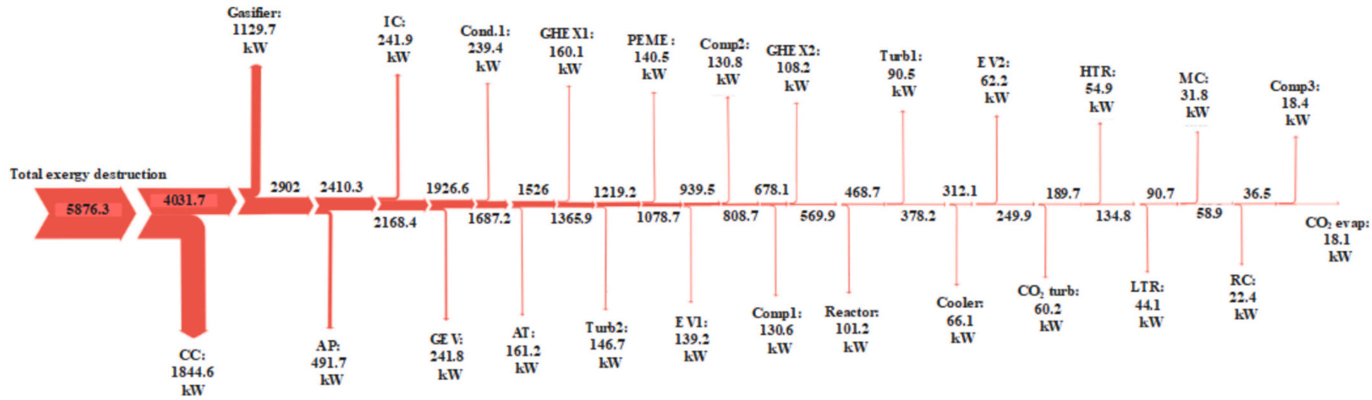

Fig. 11. Grassmann diagram illustrating the distribution of exergy flows and exergy destruction across the main components.

evaporator contribute less significantly but still present opportunities for further improvement.

Fig. 11 presents the Grassmann diagram of the exergy flows within the proposed integrated biomass–geothermal system, providing a transparent visualization of exergy distribution and degradation throughout the process. As shown in Fig. 11, the total exergy destruction of the system amounts to 5876.3 kW, with the dominant contribution arising from the CC (1844.6 kW), followed by the Gasifier (1129.7 kW) and AP (491.7 kW). Significant exergy destruction is also observed in key heat-exchange components such as IC (241.9 kW) and the GHEX1 (160.1 kW).

6.2. Parametric study

A comprehensive parametric study is performed elucidate the dynamic behavior of the proposed multigeneration system and assess the impact of essential design and operating variables. This analysis investigates how variations in selected input parameters—such as turbine inlet pressures (P_{27} and P_{29}), geothermal fluid temperature ($T_{Geofluid}$), gas turbine inlet temperature (GTIT), and the recompression SR—affect the overall system performance. The impact of these variations is evaluated across multiple key performance indicators, including net power generation (NPG), APR, normalized CO_2 emissions (NE), EE, LCOE, and sustainability index (SI). These metrics collectively reflect the thermodynamic, economic, and environmental aspects of the system's operation. It is important to note that while each parameter is analyzed, all other variables are maintained at their respective baseline values to ensure consistency and isolate the effect of the variable under investigation.

The inlet pressure of Turbine 1 (P_{27}), which governs the expansion process in the geothermal subsystem, plays a critical role in determining the performance of the proposed system. To evaluate its influence, a parametric study was conducted by varying P_{27} from 200 kPa to 600 kPa, and analyzing the corresponding variations in performance metrics, as illustrated in Fig. 12.

As observed in Fig. 12(a), increasing P_{27} initially leads to noticeable improvements in both NPG and APR. NPG increases steadily from 4011.7 kW at 200 kPa to a peak of 4093.23 kW at 490 kPa. This trend can be attributed to the enhanced expansion work achieved due to the higher inlet enthalpy of the geothermal working fluid, which allows more mechanical energy extraction through the turbines. This additional mechanical work supports increased hydrogen production in the PEM electrolyzer, which in turn enhances the ammonia synthesis rate. Accordingly, APR also rises from 588.2 kg/day to a maximum of ~ 600.28 kg/day over the same pressure range. Beyond the optimal range (around 490–500 kPa), both NPG and APR begin to plateau or show marginal declines. This behavior stems from thermodynamic limitations and component inefficiencies, where further pressurization yields diminishing returns due to increased fluid irreversibilities and constraints in turbine performance. In terms of environmental performance, NE exhibits a consistent reduction as pressure increases, dropping from 30.39 kg/GJ at 200 kPa to a minimum of approximately 29.81 kg/GJ around 500 kPa, as shown in Fig. 12(a). This trend reflects the system's improved energy utilization efficiency, leading to lower emissions per unit of generated energy.

Fig. 12(b) further illustrates the impact of P_{27} on exergy-based and economic metrics. The exergetic efficiency increases from 53.54% to a maximum of around 54.63%, confirming enhanced utilization of available energy resources with increasing turbine inlet pressure. The sustainability index also increases correspondingly from 2.16 to 2.25, affirming the system's growing environmental and energetic performance. From an economic standpoint, LCOE decreases notably from 6.58 to 6.44 cents/kWh as P_{27} increases up to 500 kPa, indicating better cost-effectiveness. This reduction is primarily attributed to increased power output without significant growth in capital or operating expenses. However, beyond this range, the improvement in LCOE becomes negligible, highlighting the existence of an optimal pressure window for economic viability.

Fig. 13 investigates the influence of Turbine 2 inlet pressure (P_{29}) on the overall performance of the system. As this turbine is part of the geothermal cycle, the inlet pressure plays a vital role in dictating the energy extraction potential from the geothermal source and subsequently affects the downstream performance of other units. As depicted in Fig. 13(a), NPG demonstrates a consistent upward trend with rising turbine inlet pressure. Specifically, the rise in power production occurs between 20 and 80 kPa, going from 3877.81 kW to 4109.88 kW. This improvement is ascribed to the higher enthalpy content and energy density of the geothermal working fluid at elevated pressures, which enhances the mechanical work output of the turbine and subsequently increases electrical generation in the downstream systems. This improvement in power generation also boosts the PEM electrolyzer's hydrogen output, thereby contributing to a rise in APR from 568.45 kg/day to 601.70 kg/day over the studied pressure range. Meanwhile, NE—expressed in kg/GJ—decline steadily from 31.49 kg/GJ at 20 kPa to 29.74 kg/GJ at 80 kPa. This downward trend is the result of increased system efficiency and better energy use, which reduces the relative amount of greenhouse gas emissions required per unit of output.

As shown in Fig. 13(b), the EE improves substantially with increasing P_{29}, rising from 51.34% to 54.90%. This is a direct outcome of more effective energy extraction and lower entropy generation in the geothermal unit, resulting in increased efficiency of geothermal heat conversion into useful work. Correspondingly, the LCOE exhibits a favorable decreasing trend, dropping from 6.78 cents/kWh at the lowest pressure to 6.42 cents/kWh at the highest pressure. This economic benefit is driven by the increased net generated electricity, which allocates the operational costs and fixed capital across a larger generation

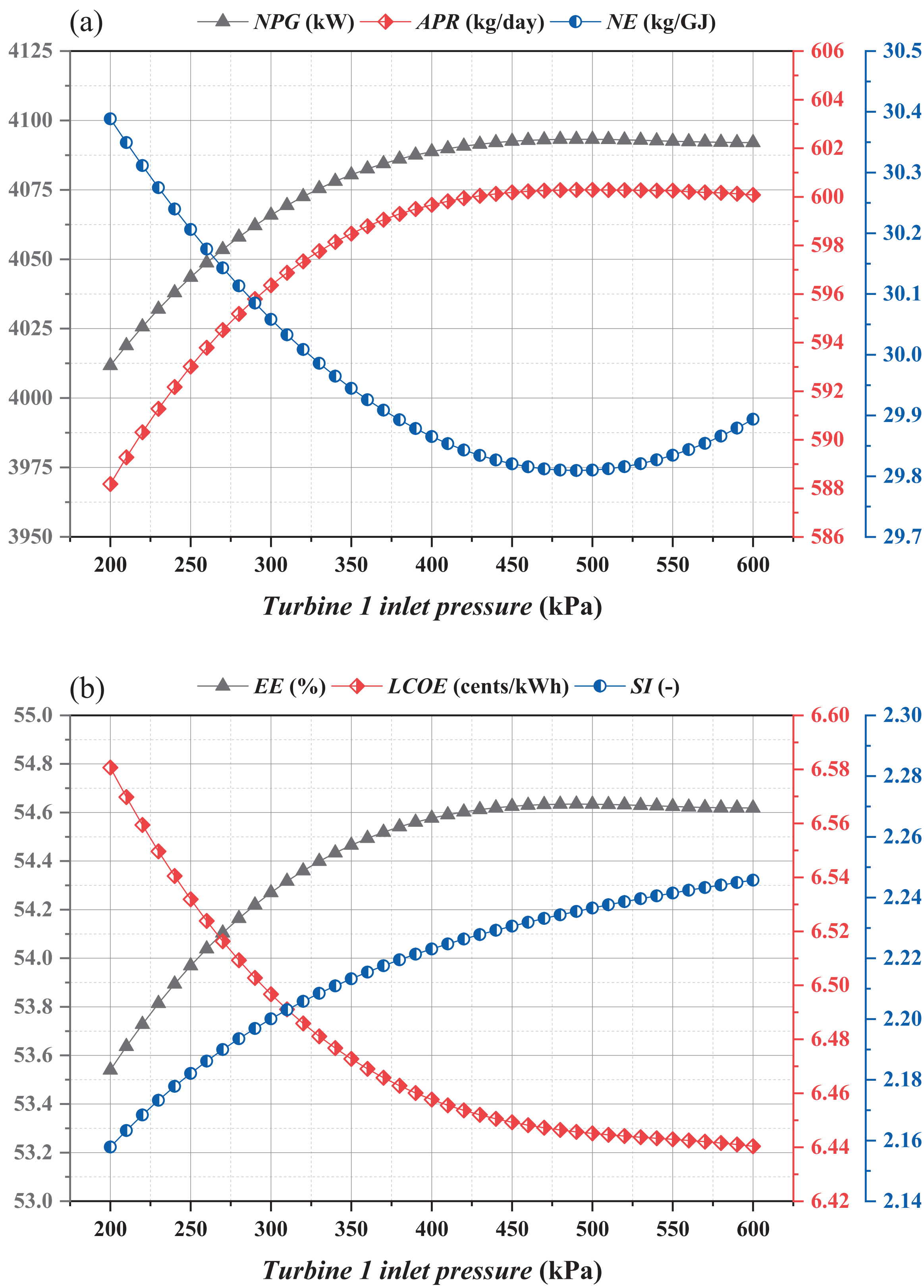

Fig. 12. Variation of the system's key performance metrics with changes in P_{27}.

capacity, thereby reducing the cost per unit of electricity. Lastly, the SI, a dimensionless measure reflecting the system's thermodynamic and environmental sustainability, increases from 2.11 to 2.24 across the studied range. This gain further emphasizes the dual benefit of improved energy performance and reduced emissions.

The geothermal fluid temperature is a critical operating parameter that directly influences the performance of the geothermal subsystem and, by extension, the overall multigeneration system. As depicted in Fig. 14(a), a continuous increase in both NPG and APR is observed with rising $T_{Geofluid}$. Specifically, the NPG improves significantly from 3763

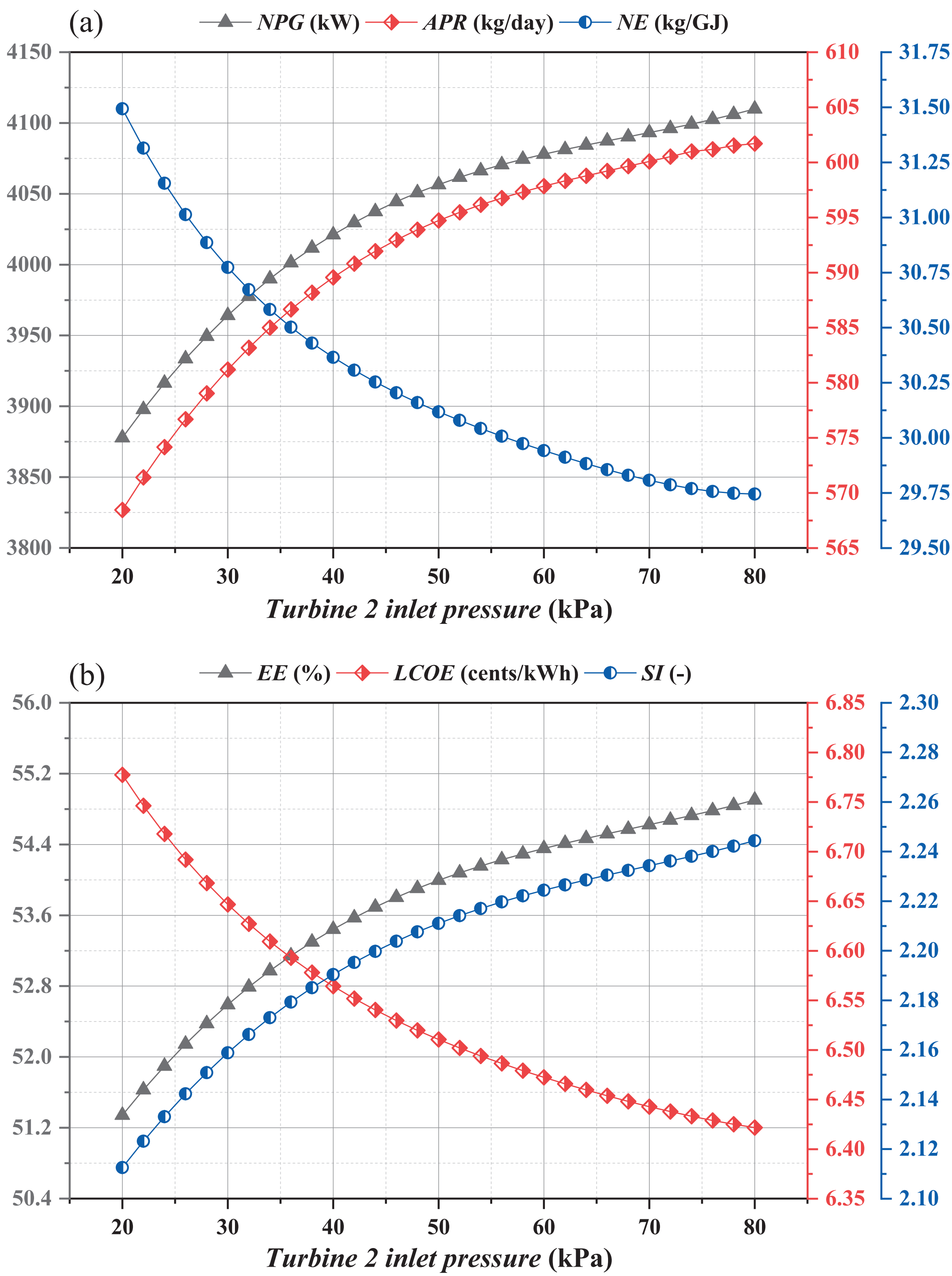

Fig. 13. Effect of P_{29} on main indicators: (a) NPG, APR, and NE; (b) EE, LCOE, and SI.

kW at 190 °C to 4291 kW at 250 °C, demonstrating enhanced energy extraction from the geothermal source. This improvement is explained by the larger thermal enthalpy content at higher fluid temperatures, which enables more effective expansion through the steam turbines and augments the mechanical work output. Consequently, more electricity is available for the PEM electrolysis process, leading to increased hydrogen production and higher ammonia synthesis. In parallel, across the temperature range being considered, the APR rises steadily from 551.6 kg/day to 629.2 kg/day, confirming the system's capacity to leverage additional thermal energy for chemical production. The environmental indicator, NE, exhibits a favorable trend by declining from 32.45 kg/GJ to 28.47 kg/GJ as temperature increases. This reduction signifies improved environmental efficiency due to higher output per unit of fuel input, thereby diluting the emissions intensity. The improvement in

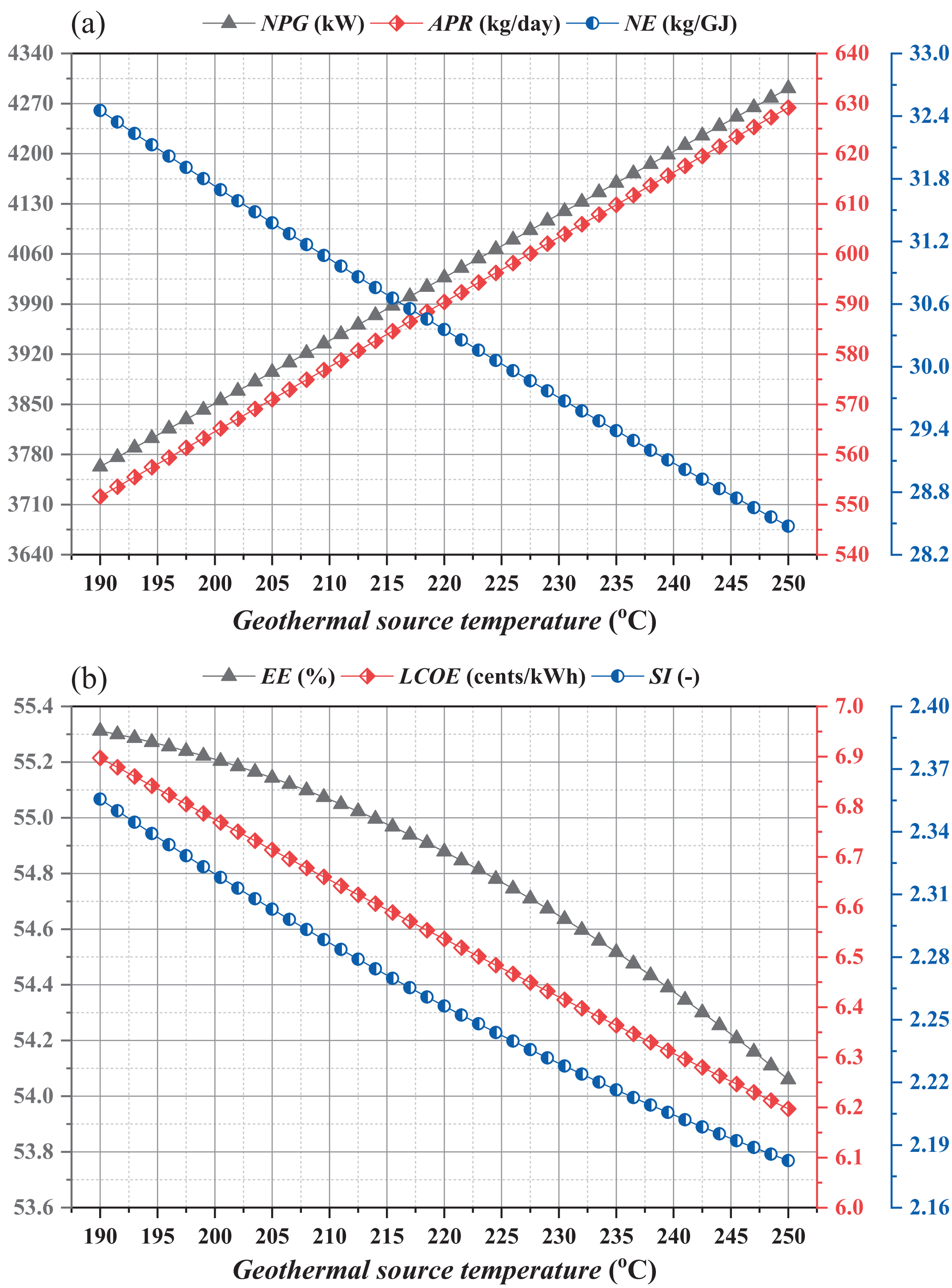

Fig. 14. Impact of geothermal fluid temperature on key performance metrics of the system.

environmental performance at higher geothermal temperatures also reflects the synergistic role of renewable heat in reducing fossil fuel reliance in the configuration.

Besides, Fig. 14(b) shows, the exergy efficiency of the system experiences a gradual decline from 55.31% to 54.06% with increasing $T_{Geo\text{-}fluid}$. This inverse trend, though subtle, suggests that while more thermal energy is available, the degree of irreversibility and entropy generation within the geothermal heat exchangers and turbines may increase at higher source temperatures, thus marginally reducing the overall second-law performance. A comparable downward trend appears in the sustainability index, which drops from 2.36 to 2.18. This behavior confirms that despite the boost in power and ammonia production, the thermodynamic quality of energy usage is slightly compromised due to elevated thermal losses at higher operating temperatures. Economically, the system benefits from a consistent reduction in LCOE, falling from 6.90 to 6.20 cents/kWh across the studied range. This improvement underscores the economic merit of operating at higher temperatures for geothermal fluid, where increased power generation reduces the unit cost of power generation. The trend highlights how leveraging low-grade geothermal resources at elevated temperatures contributes to system-wide cost optimization.

The gas turbine inlet temperature (GTIT) significantly influences the

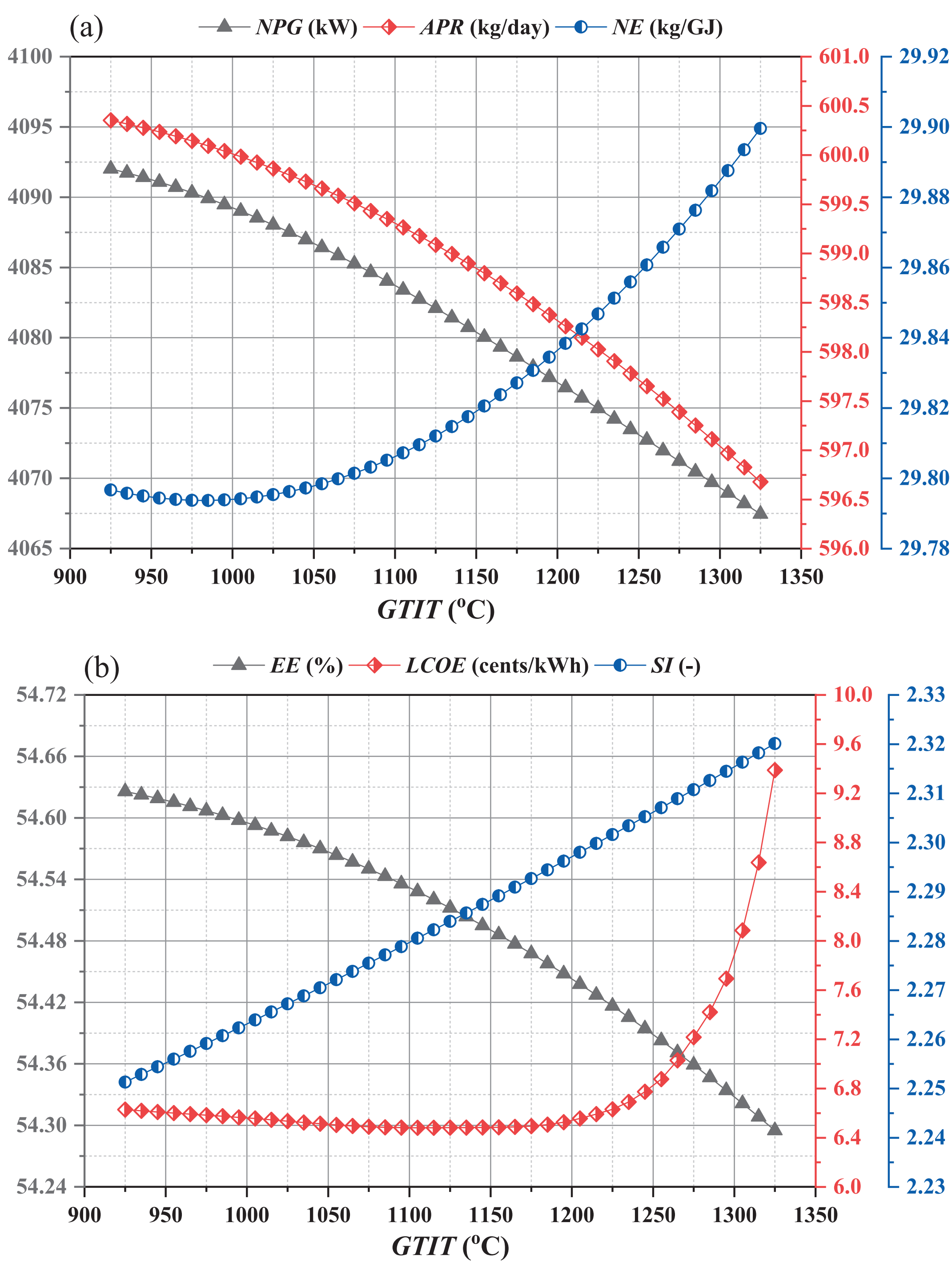

Fig. 15. Effect of GTIT on system performance: (a) NPG, APR, and NE; (b) EE, LCOE, and SI.

energy conversion efficiency and combustion behavior within the GT subsystem. Both NPG and APR gradually decline when GTIT increases, as shown in Fig. 15(a). Specifically, NPG decreases from 4092 kW at 925 °C to approximately 4067 kW at 1325 °C, while across the same range of temperature, APR falls from 600.35 kg/day to 596.68 kg/day. This inverse behavior can be attributed to the increased irreversibilities and thermal losses occurring at higher turbine inlet temperatures, which reduce the system's mechanical work output. Despite the higher combustion temperature theoretically offering more available energy, real-world constraints such as turbine material limitations, cooling requirements, and increased exhaust losses contribute to diminishing returns on system performance. In parallel, NE show a slight yet consistent increase, from 29.80 kg/GJ to 29.90 kg/GJ, indicating deteriorating environmental performance due to higher fuel consumption rates and less efficient combustion at elevated GTIT values. Fig. 15 (b) further supports these findings by demonstrating a declining trend in EE from 54.63% to 54.30%, reflecting the greater exergy destruction associated with the elevated temperatures in the GT cycle. In line with this, the SI also slightly declines, dropping from 2.25 to 2.18, signaling a less favorable balance between exergy efficiency and environmental burden. The economic aspect, represented by the LCOE, exhibits a non-linear but generally increasing trend, starting from 6.63 cents/kWh at 925 °C and reaching 9.39 cents/kWh at 1325 °C. The rise in LCOE is driven by a combination of reduced power output and increased operational inefficiencies, making electricity generation progressively more expensive at higher GTIT values.

In the recompression S-CO_2 cycle, the SR defines the fraction of CO_2 mass flow directed through the recompression branch rather than the main compressor, and it plays a significant role in shaping the thermodynamic behavior of the cycle. As shown in Fig. 16, the variation of SR from 0.55 to 0.85 demonstrates a distinct influence on the cycle's performance metrics. The NPG consistently increases with SR across the entire studied range. This improvement is attributed to the increased utilization of the high-temperature stream in the recompression path, which enhances the turbine work output and reduces the irreversibility in the recuperators. As the mass flow through the recompression branch rises, the amount of working fluid bypassing LTR decreases, allowing more effective heat recovery and thus greater energy conversion, resulting in an elevation in NPG from 3688 kW at SR = 0.55 to 3964 kW at SR = 0.85.

The S-CO_2 cycle's thermal efficiency and exergy efficiency both exhibit a non-monotonic trend with respect to SR. Initially, increasing SR improves the thermal matching within the recuperators and optimizes the distribution of irreversibility, thereby enhancing energy conversion. This leads to a rise in thermal performance from 36.7% to a peak of approximately 43.18% near SR = 0.74, and similarly, the exergy efficiency increases from 59.26% to a maximum of about 68.12%. However, beyond this optimal point, further increases in SR start to deteriorate the performance. This is mainly due to a reduction in heat recovery effectiveness, increased compressor work, and diminished temperature gradients in the HTR, which together contribute to growing internal irreversibilities and lower efficiencies. The S-CO_2 cycle's SI, indicative of the overall thermodynamic and environmental efficacy of the framework, follows a trend similar to that of the efficiencies. It increases with SR, reaching a maximum of approximately 3.72 around SR = 0.74. Beyond this value, the SI starts to decline gradually, indicating that excessively high split ratios may lead to diminished sustainability due to higher irreversibilities and suboptimal use of heat recovery resources.

6.3. Optimization results

A multi-criteria optimization was conducted to determine the ideal operating parameters for enhancing the system's thermoeconomic and ecological performance considering three key objectives: maximizing EE, maximizing APR, and minimizing the LCOE. The resulting Pareto frontier, shown in Fig. 17, illustrates the trade-offs between the conflicting aims. The points along the frontier signifies non-dominated solutions wherein enhancing on objective would inevitably means compromising others. This provides a valuable insight into the balance between energy efficiency, productivity, and cost-effectiveness. A representative optimal solution was selected from the Pareto set based on a balanced compromise between the three objectives. The corresponding optimal values for the decision variables and objective functions are summarized in Table 10. As shown, the optimal configuration includes a pressure of 432.7 kPa for the inlet of Turbine 1 inlet, pressure of 79.84 kPa for the inlet of Turbine 2, geothermal fluid temperature of 224.56 °C, GTIT of 924.12 °C, and S-CO_2 SR of 0.82. Under these operating conditions, the framework achieves an exergetic efficiency of 54.68%, a levelized cost of electricity of 6.47 cents/kWh, and an ammonia generation rate of 592.91 kg/day. This optimized performance reflects a well-balanced configuration that ensures high efficiency and ammonia productivity while maintaining a competitive electricity cost. It confirms the capability of the suggested system to deliver sustainable and economically viable energy and chemical outputs.

Fig. 18 illustrates a comparative assessment of the system's financial success over a 20-year project lifetime under three different market scenarios, defined by varying electricity (c_{elec}) and ammonia ($c_{ammonia}$) sale prices. The two key economic indicators presented are the PP and the NPV progression over time for each scenario. In the base case (c_{elec} = 0.05 \$/kWh, $c_{ammonia}$ = 0.4 \$/kg), the system reaches a break-even point around the year 2029, with a modest \$2.29 million NPV by 2044 (the conclusion of the study period). Under the moderate price scenario (c_{elec} = 0.09 \$/kWh, $c_{ammonia}$ = 0.5 \$/kg), the payback period is significantly shortened to 2027, with the NPV rising sharply thereafter to approximately \$3.92 million by 2044, indicating enhanced financial viability. The high-price scenario (c_{elec} = 0.11 \$/kWh, $c_{ammonia}$ = 0.7 \$/kg) presents the most favorable outcome, with the system recovering its capital cost by 2026 and attaining a substantial NPV of nearly \$6.53 million by the end of the project horizon. The above scenario illustrates the strong sensitivity of the framework's economic viability to product pricing,

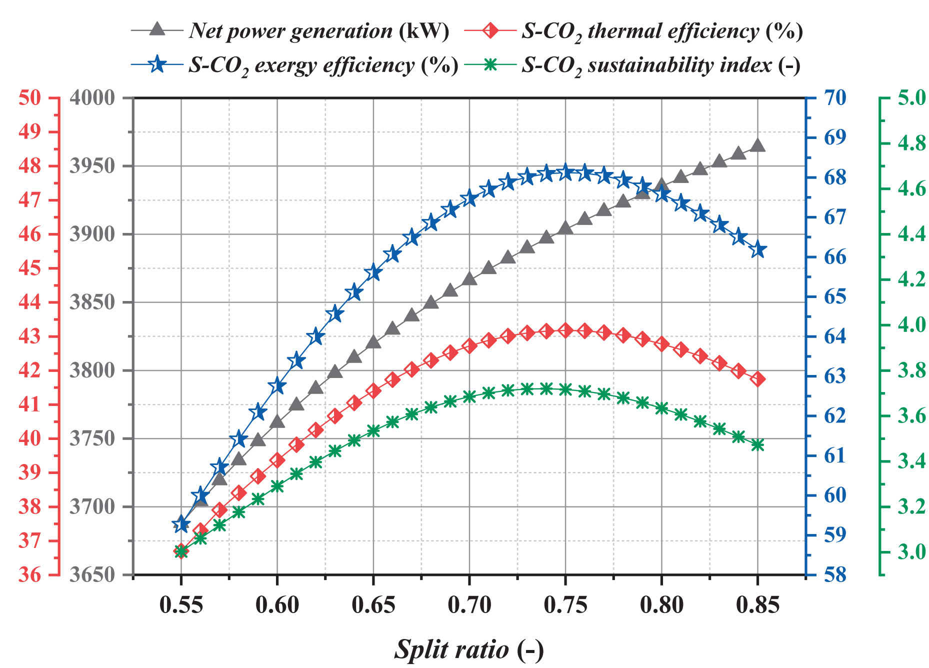

Fig. 16. Effect of GTIT on system performance: (a) NPG, APR, and NE; (b) EE, LCOE, and SI.

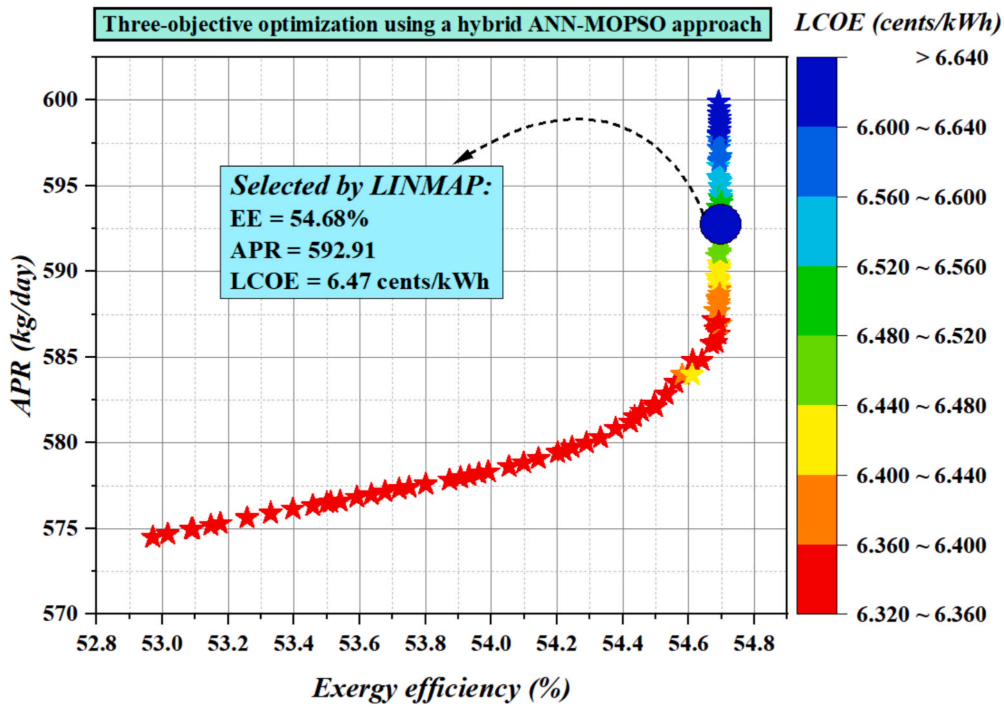

Fig. 17. Pareto frontier illustrating the trade-off between EE, APR, and LCOE in the multi-objective optimization.

Table 10
Selected design variable values and corresponding objective outcomes for the chosen Pareto-optimal solution.

Variables/Objectives	Optimal values
Turbine 1 inlet pressure, P_{27} (kPa)	432.7
Turbine 2 inlet pressure, P_{29} (kPa)	79.84
Geothermal fluid temperature, $T_{Geofluid}$ (^{o}C)	224.56
Gas turbine inlet temperature, *GTIT* (^{o}C)	924.12
S-CO_2 split ratio, *SR* (−)	0.82
Objective functions	
Exergy efficiency, EE (%)	54.68
Ammonia production rate, APR (kg/day)	592.91
Levelized cost of electricity, LCOE (cents/kWh)	6.47

particularly for ammonia.

Table 11 summarizes the economic performance metrics obtained using the exergy-based cost allocation for the non-optimized base case and the optimized configuration determined by the ANN–MOPSO algorithm. The optimization successfully reduced both levelized costs. The LCOE for the optimal system was determined to be 6.47 cents/kWh, corresponding to a 3.72% reduction relative to the initial base condition. In parallel, the LCOA also decreased, reaching 0.48 $/kg under the optimized operating parameters. These trends confirm that the multi-objective optimization not only improves the thermodynamic indicators but also enhances the overall economic attractiveness of the co-production scheme under the consistent exergy-based allocation framework.

To improve the transparency of the economic analysis, explicit component-level economic values are reported for the main units of the hydrogen/ammonia block in addition to the cost correlations. These values are evaluated at the optimized operating condition, for which the ammonia production rate is 592.91 kg/day. At this point, the corresponding hydrogen and nitrogen feed rates are 4.36 kg/h and 20.35 kg/h, respectively. Based on the economic assumptions listed in Table 4, the purchase cost and annualized cost rate of the PEM electrolyzer, hydrogen compressor, nitrogen supply unit, nitrogen compressor, ammonia synthesis reactor, recycle/circulation unit, and condenser/separator were determined and are summarized in Table 12. This breakdown makes the economic results more traceable and clearly shows the contribution of each item to the hydrogen/ammonia production section.

The main duties of the hydrogen/ammonia production section are explicitly quantified for the optimized operating condition. These include the electricity input of the PEM electrolyzer, the compression powers required for hydrogen and nitrogen, the electricity demand of nitrogen supply, the recycle/circulation duty of the ammonia loop, the cooling/condensation duty used for ammonia recovery, and the purge loss required to avoid inert accumulation in the synthesis loop. The corresponding values are summarized in Table 13.

7. Conclusions

In light of the growing demand for sustainable energy options, this study offers a novel and comprehensive approach to integrating geothermal energy, biomass gasification, PEM electrolysis, ammonia synthesis, and an S-CO_2 cycle for the co-production of ammonia and power. The proposed configuration addresses pressing global needs for clean fuels and efficient electricity generation while enhancing economic feasibility, environmental sustainability, and thermodynamic performance. Through advanced modeling and intelligent multi-objective optimization, this research provides insightful information concerning the techno-economic feasibility of such hybrid configurations. A comprehensive techno-economic and environmental assessment was carried out to explore the intricate trade-offs between production capacity, levelized electricity cost, exergy efficiency, and normalized toxic emissions. In addition, a detailed exergy destruction analysis across all subsystems identified sources of irreversibility and performance degradation. To support optimal system design, a hybrid machine learning-based framework was implemented using ANN integrated with the MOPSO algorithm. The following are the study's key conclusions:

- Analyzing exergy destruction revealed that the gas turbine-based subsystem accounted for ∼ 70.6% of total system irreversibility

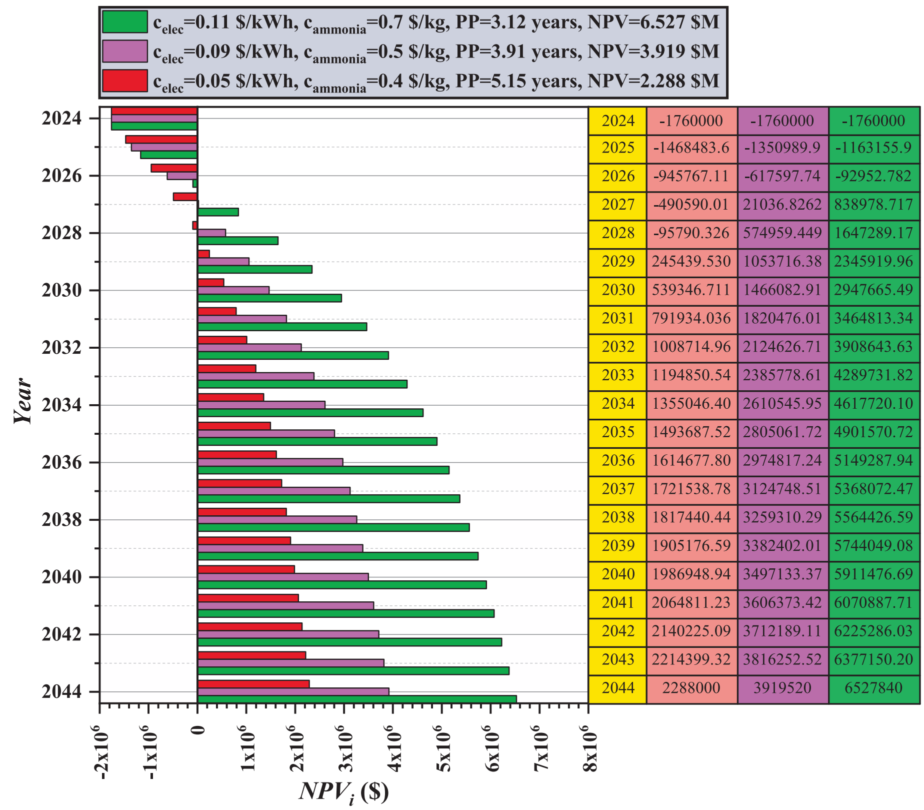

Fig. 18. Payback period and net present value comparison under three different price scenarios.

Table 11
Comparison of levelized costs for base and optimized system configurations.

Metric	Base condition	Optimized condition	Improvement (%)
LCOE (cents/kWh)	6.94	6.47	6.77
LCOA ($/kg)	0.51	0.48	5.88

Table 12
Component-level economic results for the hydrogen/ammonia block at the optimized operating point.

Component	Main basis at optimized condition	Cost rate ($/h)
PEM electrolyzer	H_2 production =4.36 kg/h	3.41
Hydrogen compressor	H_2 compression from 101.3 kPa to 10000 kPa	0.85
Nitrogen supply unit	N_2 production = 20.35 kg/h; specific electricity = 0.25kWh/kg $-N_2$	0.50
Nitrogen compressor	N_2 compression from 101.3 kPa to 10000 kPa	0.32
Ammonia synthesis reactor	NH_3 production = 24.70 kg/h	1.21
Recycle/circulation equipment	ammonia-loop recirculation and pressurization service	0.43
Condenser/separator	NH_3 cooling, condensation, and	0.46

Table 13
Duties of the hydrogen/ammonia block at the optimized operating point.

Item	Value	Unit
PEME electricity input	226.7	kW
N_2 supply electricity input	5.09	kW
H_2 compression power	9.2	kW
N_2 compression power	3.1	kW
Ammonia-loop recycle/circulation power	4.8	kW
Cooling/condensation duty	24.6	kW
Purge loss	1.0	% of loop gas
Equivalent NH_3 loss in purge	0.25	kg/h

(4148.95 kW), primarily due to combustion losses in the CC (1844.57 kW) and gasifier (1129.71 kW), while the geothermal and S-CO_2 cycles contributed 20.2% and 5.1% respectively.

- The recompression SR in the S-CO_2 cycle had a non-linear effect, with optimal performance achieved near SR = 0.74–0.76, where thermal and exergy efficiencies in the S-CO_2 cycle peaked at 43.18% and 68.12%, respectively, and net power generation approached 3900 kW.
- Increasing the inlet pressure of Turbine 1 up to ~ 480–490 kPa enhances NPG, APR, EE, and reduces LCOE and NE. Beyond this range, the performance metrics exhibit a flat or slightly declining trend due to growing irreversibilities. Notably, the lowest CO_2 emissions (~29.8 kg/GJ) occur at 480 kPa, reflecting peak environmental performance.
- Rising geothermal fluid temperature significantly boosts NPG and APR due to enhanced thermal energy extraction. NE also improves. However, EE and SI exhibit slight declines, attributed to increased irreversibilities in heat exchangers.
- Increasing GTIT from 925 °C to 1325 °C results in decreased NPG and APR, along with a slight rise in NE, indicating reduced energy conversion and higher emissions. EE gradually drops, but the SI improves slightly. LCOE remains relatively stable up to 1200 °C, then rises sharply.
- The system breaks even in 2029 under base prices, achieving $2.29 M NPV. With higher product prices, payback shifts to 2026–2027 and NPV rises to $6.53 M, showing strong sensitivity to market conditions, especially ammonia pricing.

Future research could explore the integration of pressurized solid oxide electrolysis cells (SOECs) to leverage high-temperature waste heat from the gas turbine and geothermal subsystems for more efficient hydrogen production. Additionally, implementing a cascaded ammonia recovery strategy using multi-stage condensation could enhance ammonia yield while enabling internal heat recovery for preheating feedwater or air streams. Investigating dynamic control strategies under variable geothermal and biomass feed conditions would also help improve system flexibility. Moreover, coupling the system with a thermal energy storage unit may allow load shifting and improved dispatchability. Lastly, real-time multi-objective control strategies using digital twins can be developed to dynamically optimize power-ammonia co-production under fluctuating demand and resource inputs.

CRediT authorship contribution statement

Marwa Ben Slimene: Writing – original draft, Validation, Software, Resources, Investigation, Formal analysis, Conceptualization. **Ali Basem:** Writing – review & editing, Software, Project administration, Data curation. **Naeim Farouk:** Writing – review & editing, Visualization, Validation, Software, Methodology, Investigation, Conceptualization. **Mohd Abul Hasan:** Writing – review & editing, Investigation, Funding acquisition, Data curation. **Mohamed Arbi Khlifi:** Writing – original draft, Software, Methodology, Investigation, Formal analysis, Conceptualization. **Saiful Islam:** Writing – review & editing, Supervision, Software, Methodology, Investigation. **Zukhra Atamuratova:** Visualization, Validation, Project administration. **Otabek Mukhitdinov:** Writing – original draft, Formal analysis, Data curation. **Egambergan Khudoynazarov:** Visualization, Resources, Methodology. **Ibrahim Mahariq:** Writing – review & editing, Methodology, Investigation, Conceptualization.

Funding

This research was funded by the Deanship of Research and Graduate Studies at King Khalid University under grant number RGP2/44/47.

Declaration of competing interest

The authors declare that they have no known competing financial interests or personal relationships that could have appeared to influence the work reported in this paper.

Acknowledgment

The authors extend their appreciation to the Deanship of Research and Graduate Studies at King Khalid University for funding this work through Large Research Project under grant number RGP2/44/47.

Data availability

Data will be made available on request.

References

[1] Pang L, Liu L, Zhou X, Hafeez M, Ullah S, Sohail MT. How does natural resource depletion affect energy security risk? New insights from major energy-consuming countries. Energy Strateg Rev 2024;54:101460. https://doi.org/10.1016/j.esr.2024.101460.

[2] Lale D, Pevec D. Long-term use of nuclear energy from the aspect of economy and greenhouse gas emissions. Energies 2025;18(11):2978. https://doi.org/10.3390/en18112978.

[3] Østergaard PA, Duic N, Noorollahi Y, Kalogirou S. Advances in renewable energy for sustainable development. Renew Energy 2023;219:1145–52. https://doi.org/10.1016/j.renene.2023.119377.

[4] B. Nastasi, N. Markovska, T. Puksec, N. Duić, and A. Foley, "Renewable and sustainable energy challenges to face for the achievement of Sustainable Development Goals," 2022, Elsevier. doi: 10.1016/j.rser.2022.112071.

[5] Sorrenti I, Harild Rasmussen TB, You S, Wu Q. The role of power-to-X in hybrid renewable energy systems: a comprehensive review. Renew Sustain Energy Rev 2022;165:112380. https://doi.org/10.1016/j.rser.2022.112380.

[6] Allouhi H, Allouhi A, Almohammadi KM, Hamrani A, Jamil A. Hybrid renewable energy system for sustainable residential buildings based on Solar Dish Stirling and wind Turbine with hydrogen production. Energy Convers Manag 2022;270:116261. https://doi.org/10.1016/j.enconman.2022.116261.

[7] Anya B, Mohammadpourfard M, Akkurt GG, Mohammadi-Ivatloo B. Exploring geothermal energy based systems: review from basics to smart systems. Renew Sustain Energy Rev 2025;210:115185. https://doi.org/10.1016/j.rser.2024.115185.

[8] Lee J, Kim S, You S, Park YK. Bioenergy generation from thermochemical conversion of lignocellulosic biomass-based integrated renewable energy systems. Renew Sustain Energy Rev 2023;178:113240. https://doi.org/10.1016/j.rser.2023.113240.

[9] Balali A, Moghimi M. Energy system design based on municipal solid waste gasification and SOFC for multi-demand applications through multi-heat recovery approach: 4E assessment and machine learning optimization. Process Saf Environ Prot 2025;195:106763. https://doi.org/10.1016/j.psep.2025.01.017.

[10] Olabi AG, Mahmoud M, Soudan B, Wilberforce T, Ramadan M. Geothermal based hybrid energy systems, toward eco-friendly energy approaches. Renew Energy 2020;147:2003–12. https://doi.org/10.1016/j.renene.2019.09.140.

[11] Fedakar HI, Dinçer AE, Demir A. Comparative analysis of hybrid geothermal-solar systems and solar PV with battery storage: Site suitability, emissions, and economic performance. Geothermics 2025;125:103175. https://doi.org/10.1016/j.geothermics.2024.103175.

[12] Hai T, et al. Second law evaluation and environmental analysis of biomass-fired power plant hybridized with geothermal energy. Sustain Energy Technol Assessments 2023;56:102988. https://doi.org/10.1016/j.seta.2022.102988.

[13] Toker SC. A comprehensive thermodynamic assessment of an innovative solar-geothermal driven multigeneration system for sustainable production of energy, hydrogen, freshwater, heating and cooling. Renew Energy 2025;252:123571. https://doi.org/10.1016/j.renene.2025.123571.

[14] An X, et al. Enhancing geothermal power generation: a biomass-boosted multi-generation scheme with absorption refrigeration cycles and water heating; a comprehensive exergy and techno-economic analysis. Renew Energy 2026;256:123951. https://doi.org/10.1016/j.renene.2025.123951.

[15] Y. Zhang, L. Cui, and B. Li, "Hybrid Geothermal and Biomass Energy Systems,". In: Encyclopedia of Renewable Energy, Sustainability and the Environment: Volume *1-4*, vol. 2, M. R. B. T.-E. of R. E. Rahimpour Sustainability and the Environment (First Edition), Ed., Oxford: Elsevier, 2024, pp. 209–222. doi: 10.1016/B978-0-323-93940-9.00258-9.

[16] Algburi S, et al. Optimizing smart grid flexibility with a hybrid MINLP framework for renewable integration in urban energy systems. Energy Rep 2025;14:508–23. https://doi.org/10.1016/j.egyr.2025.06.009.

[17] Geng C, Zhang T, Sun W. Hybrid solar, wind, and geothermal power generation combined with energy storage for sustainable energy management in remote buildings. J Energy Storage 2025;123:116655. https://doi.org/10.1016/j.est.2025.116655.

[18] Afshardoost A, Shamsi M. Sustainable development and optimization of a geothermal–biomass hybrid energy system for green hydrogen production. Energy Convers Manage X 2025;27:101106. https://doi.org/10.1016/j.ecmx.2025.101106.

[19] Kaur S, Kumar R, Singh K, Singh S. Systematic review of hydrogen, biomass, biogas, and solar photovoltaics in hybrid renewable energy systems: advancements, challenges, and future directions. Int J Hydrogen Energy 2025;137:160–89. https://doi.org/10.1016/j.ijhydene.2025.04.525.

[20] Mohtasim MS, Das BK, Paul UK, Kibria MG, Hossain MS. Hybrid renewable multi-generation system optimization: attaining sustainable development goals. Renew Sustain Energy Rev 2025;212:115415. https://doi.org/10.1016/j.rser.2025.115415.

[21] Hai T, El-Shafay AS, Mohammed AH, Sharma K, Rajab H. Multi-objective optimization, comparison of using different biomass fuels in hybrid energy system for electricity-distilled water production based on supercritical CO2 and humidification and dehumidfication cycles. Int J Hydrogen Energy 2024;49:252–65. https://doi.org/10.1016/j.ijhydene.2023.07.338.

[22] Yan X, Yao K, Han Y, Hou J, Mao X, Li M. Proposal of a hybrid biomass/geothermal driven multigeneration system for methanol, power, and hydrogen production: a thermodynamic and economic assessment. Energy 2025;324:135954. https://doi.org/10.1016/j.energy.2025.135954.

[23] Rabet S, Mahmoudi SMS, Yari M, Soltani S. Dual-combustion chamber cycle utilizing biomass and geothermal energy: a comprehensive economic analysis and multi-objective optimization for enhanced multi-generation. Renew Energy 2025;244:122760. https://doi.org/10.1016/j.renene.2025.122760.

[24] Özen DN, Çağlı Y. Performance analysis of a geothermal and biomass sourced power system producing hydrogen. Appl Therm Eng 2025;273:126912. https://doi.org/10.1016/j.applthermaleng.2025.126912.

[25] Yu N, Wang Q, Jin C. Multi-facet assessment-optimization of integrating a biomass-driven oxyfuel power plant, a molten carbonate fuel cell, and an innovative thermal integration process for a sustainable multigeneration task. Appl Therm Eng 2025;279:127669. https://doi.org/10.1016/j.applthermaleng.2025.127669.

[26] Xue X, Shi W, Zheng L, Wang J, Xu G, Lin X. Performance analyses of a novel compressed air energy storage system integrated with a biomass combined heat and power plant for the multi-generation purpose. Appl Therm Eng 2025;272:126403. https://doi.org/10.1016/j.applthermaleng.2025.126403.

[27] Bai H, et al. Development of a novel power and freshwater cogeneration plant driven by hybrid geothermal and biomass energy. Case Stud Therm Eng 2023;52:103695. https://doi.org/10.1016/j.csite.2023.103695.

[28] Ravi Kumar K, Krishna Chaitanya NVV. Towards sustainable energy–exploring the supercritical carbon dioxide (S-CO2) Brayton cycle for various applications: a

critical review. Int J Ambient Energy 2024;45(1):2378046. https://doi.org/10.1080/01430750.2024.2378046.
[29] Sun Y. Waste oxy-fuel combustion integrated with supercritical CO2 cycle and high-temperature electrolysis technologies for e-methanol production: a feasibility analysis. Process Saf Environ Prot 2024;185:225–38. https://doi.org/10.1016/j.psep.2024.02.086.
[30] Lv X, Lv Y, Zhu Y. Multi-variable study and MOPSO-based multi-objective optimization of a novel cogeneration plant using biomass fuel and geothermal energy: a complementary hybrid design. Energy 2023;270:126921. https://doi.org/10.1016/j.energy.2023.126921.
[31] Ben Hamida MB, Basem A, Rajab H, Othayq MM. Dynamic optimization of a solar–sCO2–CAES hybrid energy system: Integration of green hydrogen production and AI-based energy management. Int J Hydrogen Energy 2025;146:149888. https://doi.org/10.1016/j.ijhydene.2025.06.078.
[32] Abdelghafar MM, Hassan MA, Kayed H. Direct integration of supercritical carbon dioxide-based concentrated solar power systems and gas power cycles: advances and outlook. Appl Therm Eng 2025;269:126064. https://doi.org/10.1016/j.applthermaleng.2025.126064.
[33] Zhu C, et al. An innovative process design and multi-criteria study/optimization of a biomass digestion-supercritical carbon dioxide scenario toward boosting a geothermal-driven cogeneration system for power and heat. Energy 2024;292:130408. https://doi.org/10.1016/j.energy.2024.130408.
[34] Lan P, et al. Comparison of different hydrogen-ammonia energy conversion pathways for renewable energy supply. Renew Energy 2024;227:120602. https://doi.org/10.1016/j.renene.2024.120602.
[35] Yue M, Lambert H, Pahon E, Roche R, Jemei S, Hissel D. Hydrogen energy systems: a critical review of technologies, applications, trends and challenges. Renew Sustain Energy Rev 2021;146:111180. https://doi.org/10.1016/j.rser.2021.111180.
[36] Ojelade OA, Zaman SF, Ni BJ. Green ammonia production technologies: a review of practical progress. J Environ Manage 2023;342:118348. https://doi.org/10.1016/j.jenvman.2023.118348.
[37] Khalid Ratib M, Muttaqi KM, Islam MR, Sutanto D, Agalgaonkar AP. Electrical circuit modeling of proton exchange membrane electrolyzer: the state-of-the-art, current challenges, and recommendations. Int J Hydrogen Energy 2024;49:625–45. https://doi.org/10.1016/j.ijhydene.2023.08.319.
[38] Bozgeyik A, Altay L, Hepbasli A. Energetic, exergetic, exergoeconomic, environmental and sustainability analyses of a solar, geothermal and biomass based novel multi-generation system for production of power, hydrogen, heating, cooling and fresh water. Process Saf Environ Prot 2023;177:400–15. https://doi.org/10.1016/j.psep.2023.07.018.
[39] Wang Z, et al. Hydrogen production from biomass: a review combined with bibliometric analysis. Int J Hydrogen Energy 2025;117:271–91. https://doi.org/10.1016/j.ijhydene.2025.03.158.
[40] Yin N. Enhancing energy efficiency and reducing emissions in a novel biomass-geothermal hybrid system for hydrogen/ammonia production using machine learning and multi-level heat recovery. Int J Hydrogen Energy 2024;92:959–74. https://doi.org/10.1016/j.ijhydene.2024.10.343.
[41] Yilmaz F. An innovative study on a geothermal based multigeneration plant with transcritical CO2 cycle: thermodynamic evaluation and multi-objective optimization. Process Saf Environ Prot 2024;185:127–42. https://doi.org/10.1016/j.psep.2023.11.025.
[42] Khoshgoftar Manesh MH, Davadgaran S, Mousavi Rabeti SA, Blanco-Marigorta AM. Feasibility study of green ammonia and electricity production via an innovative wind-solar-biomass polygeneration system. Appl Energy 2025;384:125467. https://doi.org/10.1016/j.apenergy.2025.125467.
[43] Shamsi M, Karami B, Cheraghdar A, Mousavian S, Makki M, Rooeentan S. Evaluation of an environmentally-friendly poly-generation system driven by geothermal energy for green ammonia production. Fuel 2024;365:131037. https://doi.org/10.1016/j.fuel.2024.131037.
[44] Tang T, Li B, Lu M, Feng Y, Wang J. Synergistic geothermal energy and ammonia fuel cell utilization towards sustainable power, cooling, and freshwater production; an exergoeconomic, exergoenvironmental, and technoeconomic analysis. Renew Energy 2025;241:122244. https://doi.org/10.1016/j.renene.2024.122244.
[45] Yilmaz F, Ozturk M, Selbas R. A parametric examination of the energetic, exergetic, and environmental performances of the geothermal energy-based multigeneration plant for sustainable products. Int J Hydrogen Energy 2025;143:947–57. https://doi.org/10.1016/j.ijhydene.2024.12.236.
[46] Jia Q, et al. A novel cascade heat design for a geothermal energy-based combined power plant in integration with water electrolysis and ammonia synthesis processes: comprehensive thermo-environ-economic analyses. Energy 2024;311:133383. https://doi.org/10.1016/j.energy.2024.133383.
[47] Khoshgoftar Manesh MH, Davadgaran S, Mousavi Rabeti SA. New procedure for designing an innovative biomass-solar-wind polygeneration system for sustainable production of power, freshwater, and ammonia using 6E analyses, carbon footprint, water footprint, and multi-objective optimization. Renew Energy 2024;230:120802. https://doi.org/10.1016/j.renene.2024.120802.
[48] Anand A, Kachhap A, Gautam S. Synergistic effect of coal and biomass gasification and organo-inorganic elemental impact on gasification performance and product gas. Energy 2023;282:128662. https://doi.org/10.1016/j.energy.2023.128662.
[49] Wang J, et al. A renewable multigeneration system based on biomass gasification and geothermal energy: techno-economic analysis using neural network and Grey Wolf optimization. J Energy Storage 2024;104:114519. https://doi.org/10.1016/j.est.2024.114519.
[50] Aich W, et al. Comprehensive study and design optimization of a hybrid solar-biomass system for enhanced hydrogen production and carbon dioxide reduction. Appl Therm Eng 2024;256:124074. https://doi.org/10.1016/j.applthermaleng.2024.124074.
[51] Ahmadi P, Dincer I, Rosen MA. Thermodynamic modeling and multi-objective evolutionary-based optimization of a new multigeneration energy system. Energy Convers Manage 2013;76:282–300. https://doi.org/10.1016/j.enconman.2013.07.049.
[52] Mehrenjani JR, Gharehghani A, Nasrabadi AM, Moghimi M. Design, modeling and optimization of a renewable-based system for power generation and hydrogen production. Int J Hydrogen Energy 2022;47(31):14225–42. https://doi.org/10.1016/j.ijhydene.2022.02.148.
[53] You J, Xiao R, Alotaibi MA, Chauhdary ST, Ji T. Integrating an innovative geothermal-driven multigeneration approach and LNG cold energy utilization process for sustainable energy supply, producing hydrogen, power, heating, and cooling. Process Saf Environ Prot 2025;196:106904. https://doi.org/10.1016/j.psep.2025.106904.
[54] I. G. Kevrekidis and S. Y. Shvartsman, “Chemical Reactor Analysis and Design Fundamentals: Jim Rawlings and John Ekerdt; Nob Hill Publishing, Madison, WI, 2002. ISBN 0-615-11884-4,” Chem. Eng. Sci. 59(10) 2004 2123–2124. doi: Doi: 10.1016/j.ces.2003.12.030.
[55] Kazemi H, Lotfollahi A, Moghimi M. A net-zero carbon emission multi-generation system for green ammonia production: comprehensive analysis and ANN-assisted optimization using moth flame optimizer. Int J Hydrogen Energy 2025;137:303–22. https://doi.org/10.1016/j.ijhydene.2025.04.510.
[56] Hasanzadeh A, Chitsaz A, Ghasemi A, Mojaver P, Khodaei R, Alirahmi SM. Soft computing investigation of stand-alone gas turbine and hybrid gas turbine–solid oxide fuel cell systems via artificial intelligence and multi-objective grey wolf optimizer. Energy Rep 2022;8:7537–56. https://doi.org/10.1016/j.egyr.2022.05.281.
[57] Emadi MA, Mahmoudimehr J. Modeling and thermo-economic optimization of a new multi-generation system with geothermal heat source and LNG heat sink. Energy Convers Manage 2019;189:153–66. https://doi.org/10.1016/j.enconman.2019.03.086.
[58] Dong RE, et al. A heat recovery-based ecofriendly solar thermal-driven electricity/hydrogen/freshwater multigeneration scheme using LNG regasification: energy, exergy, economic, and environmental (4E) analysis. Case Stud Therm Eng 2024;53:103853. https://doi.org/10.1016/j.csite.2023.103853.
[59] Mehrenjani JR, Gharehghani A, Sangesaraki AG. Machine learning optimization of a novel geothermal driven system with LNG heat sink for hydrogen production and liquefaction. Energy Convers Manage 2022;254:115266. https://doi.org/10.1016/j.enconman.2022.115266.
[60] Bejan A, Tsatsaronis G, Moran MJ. Thermal Design and Optimization. John Wiley & Sons; 1995.
[61] Ismail MA, et al. Design and optimization of a modified solar-driven energy system utilizing advanced heat recovery methods for electricity and hydrogen production in sustainable urban applications. Process Saf Environ Prot 2025;195:106720. https://doi.org/10.1016/j.psep.2024.12.101.
[62] Alirahmi SM, Assareh E, Pourghassab NN, Delpisheh M, Barelli L, Baldinelli A. Green hydrogen & electricity production via geothermal-driven multi-generation system: thermodynamic modeling and optimization. Fuel 2022;308:122049. https://doi.org/10.1016/j.fuel.2021.122049.
[63] Rong Q, et al. Environmental, financial, and technological viability of based on a Grid/PV/battery/wind/electrolyzer/biogas hybrid configuration for producing energy and hydrogen. Int J Hydrogen Energy 2025;103:836–50. https://doi.org/10.1016/j.ijhydene.2025.01.249.
[64] Chen H, Alsenani TR, Ahmad SF, Asiri M, Zhang Y. Thermodynamic, exergo-environmental, and thermoeconomic assessment of a high-capacity heat and power generation system with hydrogen production: a case study on municipal solid waste combustion, geothermal fluid utilization, parametric sensitivity analysis, and integrated CO2 capture. Process Saf Environ Prot 2025;198:107163. https://doi.org/10.1016/j.psep.2025.107163.
[65] Li S, Leng Y, Nutakki TUK, Abdullaev S, Fouad Y, Alhadrawi M. Intelligent optimization of eco-friendly H2/freshwater production and CO2 reduction layout integrating GT/rankine cycle/absorption chiller/TEG unit/PEM electrolyzer/RO section. Process Saf Environ Prot 2024;189:204–18. https://doi.org/10.1016/j.psep.2024.06.062.
[66] Singh PK, et al. Waste heat recovery cycles integration into a net-Zero emission solar-thermal multi-generation system; Techno-economic analysis and ANN-MOPSO optimization. Case Stud Therm Eng 2025;66:105690. https://doi.org/10.1016/j.csite.2024.105690.
[67] Muhammed T. Optimized energy efficient reactive distillation for octane upgrading with economic and environmental considerations. Fuel 2024;378:132994. https://doi.org/10.1016/j.fuel.2024.132994.
[68] Basem A, et al. CO2 emission reduction by geothermal-driven CCHP tailored with turbine bleeding and regeneration CHP; economic/multi-aspect comparative analysis with GA-based optimization. Results Eng 2024;23:102646. https://doi.org/10.1016/j.rineng.2024.102646.
[69] Yang C, et al. Optimized integration of solar energy and liquefied natural gas regasification for sustainable urban development: Dynamic modeling, data-driven optimization, and case study. J Clean Prod 2024;447:141405. https://doi.org/10.1016/j.jclepro.2024.141405.
[70] Halawani RF, et al. An advanced heat design-CO2 capture network for an oxy-biogas fuel combustion cycle combined with a CAES-based method for peak shaving: an artificial intelligent-driven optimization. Renew Energy 2025;242:122474. https://doi.org/10.1016/j.renene.2025.122474.
[71] Cao Y, Dhahad HA, Sharma K, Anqi AE, El-Shafay AS, Najat Ahmed A. Comprehensive thermodynamic and economic analyses and optimization of a

novel poly-generation setup utilizing solar and geothermal sources. Appl Therm Eng 2022;207:118133. https://doi.org/10.1016/j.applthermaleng.2022.118133.

[72] Cao Y, Dhahad HA, Hussen HM, Anqi AE, Farouk N, Issakhov A. Development and tri-objective optimization of a novel biomass to power and hydrogen plant: a comparison of fueling with biomass gasification or biomass digestion. Energy 2022;238:122010. https://doi.org/10.1016/j.energy.2021.122010.

[73] Algburi S, et al. The role of artificial intelligence in accelerating renewable energy adoption for global energy transformation. Unconv Resour 2025;8:100229. https://doi.org/10.1016/j.uncres.2025.100229.

[74] Azamovich AT, et al. Machine learning-based fault detection and classification in microgrid. J. Oper. Autom. Power Eng. 2024;12(Special Issue):43–52. https://doi.org/10.22098/joape.2025.16912.2315.

[75] Karkon E, Liravi M, Georges L, Li J, Novakovic V. Design of a hybrid solar and biomass-based energy system integrated with near-zero energy building: techno-environment investigation and multicriteria optimization. Process Saf Environ Prot 2025;193:26–42. https://doi.org/10.1016/j.psep.2024.11.018.

[76] Ioroi T, Yasuda K, Siroma Z, Fujiwara N, Miyazaki Y. Thin film electrocatalyst layer for unitized regenerative polymer electrolyte fuel cells. J Power Sources 2002;112 (2):583–7. https://doi.org/10.1016/S0378-7753(02)00466-4.

[77] M. K. Lundgren, "Incoporating Ammonia Synthesis for an Offshore Gas-to-Liquid Process," 2016, NTNU.

[78] Zainal ZA, Ali R, Lean CH, Seetharamu KN. Prediction of performance of a downdraft gasifier using equilibrium modeling for different biomass materials. Energy Convers Manage 2001;42(12):1499–515. https://doi.org/10.1016/S0196-8904(00)00078-9.

[79] Alauddin ZAZ. Performance and characteristics of a biomass gasifier system. Cardiff: University of Wales; 1996.

[80] Wu C, Wang S, Feng X, Li J. Energy, exergy and exergoeconomic analyses of a combined supercritical CO2 recompression Brayton/absorption refrigeration cycle. Energy Convers Manage 2017;148:360–77. https://doi.org/10.1016/j.enconman.2017.05.042.

[81] Algburi S, et al. Predictive modeling of building energy consumption and thermal comfort for decarbonization in construction and retrofitting. Results Eng 2025;26:105475. https://doi.org/10.1016/j.rineng.2025.105475.

[82] Bai Y, Wang B, Cheng L. A comprehensive thermodynamic, economic, and environmental analysis of a novel parabolic trough solar-driven multigeneration system for generating power, hydrogen, and freshwater. Process Saf Environ Prot 2024;184:227–47. https://doi.org/10.1016/j.psep.2024.01.086.